Journal of the Meteorological Society of Japan

EARLY ONLINE RELEASE

The DOI for this manuscript is
DOI:10.2151/jmsj.2025-014
J-STAGE Advance published date: January 21, 2025
The final manuscript after publication will replace the preliminary version at the above DOI once it is available.

Maintenance Mechanisms of Orographic Quasi-Stationary Convective Band Formed over the Eastern Part of Shikoku, Japan

Akira NISHII[1]

Institute for Space-Earth Environmental Research, Nagoya University, Nagoya, Japan

Graduate School of Environmental Studies, Nagoya University, Nagoya, Japan

Taro SHINODA

Institute for Space-Earth Environmental Research, Nagoya University, Nagoya, Japan

and

Koji SASSA

Faculty of Science and Technology, Kochi University, Kochi, Japan

December 28, 2024

----

1) Corresponding author: Akira NISHII, Institute for Space-Earth Environmental Research, Nagoya University, Furo-cho, Chikusa-ku, Nagoya 464-8601, Japan.
Email: nishii.akira@nagoya-u.jp

Abstract

This study examines the maintenance mechanisms of Muroto Lines, a south-north oriented quasi-stationary convective band (QSCB) that appeared from the Muroto Peninsula in eastern Shikoku, Japan. The analysis area is characterized by complex orography, where many small-scale ridges are embedded in larger-scale ridges. We focused on two cases of Muroto Lines with differing depth of convective clouds: Case 1 (12–20 Japan Standard Time (JST; UTC+9 h) on July 3, 2018) and Case 2 (16–21 JST on August 15, 2018).

In both cases, atmospheric environments were characterized by warm-moist and conditionally unstable lowest-level inflows (below 600 m in height) between east-southeasterly and south-southeasterly, and high humidity below the middle troposphere (600 hPa). Both cases exhibited back-building structures; convective cells were continuously generated at the southernmost tip of the Muroto Lines and advected northward by southerly wind 2–4 km in height. The convective cells were generated over a small-scale ridge oriented from south-southwest to north-northeast due to upslope lifting when the lowest-level wind was east-southeasterly. On the other hand, when the wind was southeasterly or south-southeasterly, convergence at the eastern foot of the ridge, resulting from deflected flow at the ridge combined with undeflected flow, could trigger the convective cells. Convergence at small-scale concave valleys and the lowest-level inflow with easterly components could further develop the Muroto Lines. Vertical structures of the Muroto Lines showed that the strongest rainfall in Case 1 (Case 2) was primarily caused by relatively shallow (deep) convective cells, suggesting the importance of the collision-coalescence of raindrops (melting of graupel). Intense rainfall was also produced in the developing stage of convective cells through the collision-coalescence of raindrops in both cases. This study suggests the importance of small-scale orographic effects and cross-QSCB lowest-level inflow for the maintenance of orographic QSCBs in warm-moist environments.

Keywords mesoscale convective system; localized heavy rainfall; quasi-stationary convective band; orographic precipitation

1. Introduction

The largest rainfall accumulation is caused when the strongest rainfall occurs for the longest time (Chappel 1986; Doswell et al. 1996). Such rainfall can be caused by precipitation systems with strong rainfall intensity and slow system motion. A quasi-stationary convective band (QSCB), which is a formation mode of line-shaped mesoscale convective systems (MCSs) that produces heavy rainfall in nearly the same area for longer than a few hours, has caused historical heavy rainfall events (e.g., Kawano and Kawamura 2020; Araki et al. 2021) because of its intense precipitation and high stationarity. Kato (2020) showed that half of the heavy rainfall events that occurred in Japan had line-shaped heavy rainfall areas (50–300 km in length and 20–50 km in width). To improve forecasting skills for heavy rainfall events, it is important to understand the factors behind the intense rainfall and stationarity of QSCBs.

Many previous studies have shown favorable atmospheric factors for the maintenance of QSCBs (e.g., Unuma and Takemi 2016a and b; Bluestein and Jain 1985; Kato 2020). Kato (2020) suggested six favorable environmental factors for diagnostic forecasts of QSCBs based on heavy rainfall events brought by them in Japan. However, Kato (2020) also noted that QSCBs do not always appear in areas where all the favorable conditions are met. Numerical studies (Kato and Aranami 2005; Kato 2020) have demonstrated that the representation of QSCBs is highly sensitive to the low-level wind fields. The low- and mid-level wind directions are also important in determining the orientation of QSCBs (e.g., Yoshizaki et al. 2000; Morotomi et el. 2012; Oue et al. 2014). Further investigations into the atmospheric conditions of QSCBs that occur at various locations are required to identify the environmental factors for the maintenance of QSCBs.

The internal structure of QSCBs can vary with the vertical wind shear between the low and middle troposphere. Seko and Nakamura (2003) classified meso-β scale line-shaped rainfall systems into three types based on their internal structures: 1) squall line (SL) type, characterized by continuously generated cells along a stationary localized front; 2) back-building (BB) type, maintained by convective cells generated at the upstream side advected to the downstream side; and 3) back-and-side building (BSB) type, similar to BB-type but with additional convective cells generated at the lateral side of the line-shaped rainfall systems. They showed that SL-, BB-, and BSB-type line-shaped rainfall systems appeared when the mid-level wind direction was opposite, the same, or perpendicular to the low-level wind direction, respectively. BB-type QSCBs frequently cause localized heavy rainfall events (e.g., Ogura 1990; Kato 2020; Schumacher and Johnson 2005). Schumacher and Johnson (2005) reported that BB-type MCSs in the U.S. were maintained by mesoscale and storm-scale processes (particularly storm-generated cold pools) rather than synoptic boundaries. However, cold pools can play a minor role in the BB-type QSCBs that occur in warm and moist environments (Kato 1998; Gascón et al., 2016; Kawano and Kawamura 2020). Instead of cold pools, other forcings such as orographic effects can be essential for maintaining QSCBs.

Orographic effects usually play an essential role in the maintenance of QSCBs formed over and near mountainous regions. However, specific orographic effects can vary according to various factors, such as the atmospheric environment and the shape of orography. Houze (2012) categorized the orographic effects on precipitating clouds into six main types: upslope flow, diurnal forcing, pre-existing cloud passage over small terrain features, seeder-feeder mechanism, lee-side wave triggering, blocking effects, and capping effect. The upslope lifting of warm-moist airflow at mountain ranges is a typical maintenance mechanism of heavy orographic rainfall (e.g., Pontrelli et al., 1999; Morotomi et al. 2012). The blocked and deflected flow around large-scale mountain ranges (which may be larger than 100 km on a horizontal scale) can maintain QSCBs by forming low-level convergence with the undeflected flow from the ocean (Watanabe and Ogura 1987; Yu and Hsieh 2009). Barrett et al. (2015) found that only three of 21 ensemble members reproduced the orographic QSCB formed in the central part of the U.K., and that the QSCB was reproduced when the low-level wind flowed around the upstream mountain (50 km in horizontal length) and converged on its lee side. Small-scale orography (less than 20 km in horizontal length and 500–1500 m in height) can also play a key role in the maintenance and enhancement of orographic QSCBs, particularly in warm and moist environments where the level of free convection (LFC) is very low (Gascón et al., 2016). Yoshizaki et al. (2000) found that upslope lifting over a ridge on the Nagasaki Peninsula (600 m maximum height and 20 km horizontal length) located on the north part of Kyushu Island in Japan triggered an orographic QSCB called the Nagasaki Line. Kato (2005) statistically revealed that the Nagasaki Line can be maintained during the Baiu season when the low-level wind direction is southwesterly and the wind speed at the 850 hPa level is between 5 and 25 m s^{-1}. Morotomi et al. (2012) suggested that convergence in a small-scale concave valley, opened in the direction of low-level south-southeasterly wind, contributed to the further development of QSCB formed along the Ibuki-Suzuka Mountains (900 m maximum height and 20 km horizontal length) in central Japan. These studies suggest that orographic effects contributing to the maintenance of QSCBs are highly sensitive to low-level wind fields. Because orography usually has complex small-scale features, investigating the orographic features and low-level winds that contribute to the maintenance of orographic QSCBs occurred in various regions can enhance our understanding of their maintenance mechanisms.

The target of the present study is a south-north oriented QSCBs that maintained over the eastern part of Shikoku, Japan. We focus on this QSCB because it brought intense rainfall in the same area multiple times over complex orography. We named this QSCB the Muroto Line, as the southernmost part of the line-shaped precipitation system is located on the Muroto Peninsula (Figs. 1b–d). In this study, we analyze two cases of the Muroto Lines. As Fig. 1 detailed later, these cases maintained in nearly the same area but exhibited different characteristics in their vertical structures (Fig. 2). The first case (Case 1) occurred from 12 Fig. 2 to 20 Japan Standard Time (JST; UTC+9 h) on July 3, 2018 (Fig. 1c). This case is characterized by two lines of heavy rain areas which have been caused by the shifting of the maintenance location. Case 2 maintained from 16 to 21 JST on August 15, 2018 (Fig. 1d). In this case, the Muroto Line maintained in the same location throughout the event. The maximum accumulated rainfall in each case was very high (309 mm for 8 hours in Case 1 and 422 mm for 5 hours in Case 2), although the horizontal scales of the heavy rain area of the Muroto Lines (50 km in length and 10 km in width) were smaller than those brought by the QSCBs frequently focused on in Japan (e.g., Kato 2020; Hirockawa et al. 2020). Unuma and Murata (2012) statistically investigated the QSCBs that appeared over Shikoku and identified the Muroto Line when the wind direction at 850 hPa was southeasterly. Umemoto et al. (2005) analyzed the Muroto Line maintained for 20 hours on July 31 and August 1, 2004, and concluded that upslope lifting at the orography in the Moroto Peninsula played a key role in maintaining the Muroto Line. However, the mechanisms that determine the maintenance locations of Muroto Line remain unclear.

This study focuses on the role of small-scale orography in the maintenance of the Muroto Lines, which has not been investigated in the previous studies but can play a key role in their maintenance. This focus is relevant because the eastern part of Shikoku is characterized by complex orography. The orography can be largely divided into two regions at 33.7°N (Fig. 1b): the west-east oriented Shikoku Main Ridge (maximum height of approximately 2000 m) and the south-north oriented main ridge (SN Main Ridge; the maximum height of approximately 1400 m). Many small-scale ridges with various orientations were embedded in both main ridges. For example, in the southernmost part of the Muroto Peninsula, a steep small-scale ridge (SR in Fig. 1b; 15 km length, 5 km wide, and 750 m high) oriented from south-southwest to north-northeast was embedded in the SN Main Ridge. The southern part of the SR ridge protrudes slightly to the east compared with its northern part. Some ridges formed small-scale concave valleys (e.g., CV1 and CV2 in Fig. 1b). Such small-scale orographic features may contribute to the maintenance of the Muroto Line because QSCBs are usually maintained by mesoscale and storm-scale (O(10 km) for the Muroto Line) processes (Schumacher and Johnson 2005).

The vertical structure of the Muroto Line differs between the two cases. Figure 2 shows snapshots of the radar horizontal reflectivity (Z_h) at a height of 2 km and vertical cross sections along the Muroto Lines observed by the Japan Meteorological Agency (JMA) Murotomisaki radar. Although the horizontal distribution of Z_h was almost identical in both cases (Figs. 2a and 2c), the echo-top height in Case 2 was higher than that in Case 1 (Figs. 2b and 2d). Recent studies (e.g., Hamada et al. 2015; Hamada and Takayabu 2018; Sohn et al. 2013) have shown that intense rainfall can also be produced by relatively shallow convective cells through the collision-coalescence of raindrops (warm-rain processes), which differs from the generally accepted heavy-rain-producing processes where the melting of graupel particles in deep convective clouds produces intense rainfall (cold-rain processes). The present study also documents the differences in the vertical Z_h structures between the two cases, which can be helpful to understand the heavy-rain-producing processes of orographic QSCBs.

The purpose of this study is to clarify the maintenance mechanisms of the two cases of Muroto Lines and document the differences in their vertical structures. We note that the focus of this study is on QSCBs, rather than the resulting rainfall area. Section 2 describes the data and methods used in this study. Section 3 provides an overview of the two cases. Sections 4 and 5 present the results and discussions, respectively. Section 6 summarizes the present study.

2. Data and Method

To analyze the horizontal structures of the Muroto Lines, we used Extended RAdar Information Network (XRAIN) composite rainfall intensity data provided by the Ministry of Land, Infrastructure, Transport, and Tourism (MLIT) in Japan. This dataset comprises rainfall intensity at a height of approximately 2 km estimated from Z_h and the specific differential phase (K_{dp}) collected by MLIT C- and X-band weather radars (mostly dual-polarized) installed across Japan. The horizontal and temporal resolutions of the dataset are 250 m and 1 min, respectively. We note that unrealistic rainfall intensity sometimes appears within 10 km of one of the XRAIN C-band polarimetric radars located in the northern part of the Muroto Line in Case 1 (33.89°N, 134.24°E; a yellow triangle in Fig. 1c).

We also utilized the Plan Position Indicator (PPI) data of Z_h observed using the C-band single-polarimetric JMA Murotomisaki radar located at the southernmost tip of the Muroto Peninsula (blue triangle in Fig.1c) to investigate the vertical structures of the Muroto Lines. Note that this radar is not part of XRAIN. We used 12 elevation angles of PPIs ranging from 0.4° to 25.0°, observed every 10 min. We manually excluded beam blockage areas that appeared at the lower elevation angles of the PPIs (0.4°, 1.2°, and 1.9°). Z_h was corrected for rainfall attenuation with a relation $A = \int_0^r 2\,K(r)\,dr$; where A is total rainfall attenuation along a beam path, r is a distance from the radar, K represents one-way specific attenuation defined by $K = 0.0018\,R^{1.05}$ (Doviak and Zrnić 1992), R is rainfall intensity estimated from Z_h (mm^6 m^{-3}) using the relationship $Z_h = 200\,R^{1.6}$. The PPI data were interpolated to constant altitude plan position indicator (CAPPI) grids using the method of Cressman (1959) with a horizontal resolution of 1 km and a vertical resolution of 0.5 km. We conducted echo-top height and contoured frequency by altitude diagram (CFAD, Yuter and Hauze 1995) analyses using CAPPI data. To capture the vertical structure of intense precipitation, a CFAD analysis was conducted on vertical columns where Z_h was 35 dBZ or greater at a height of 1.5 km. Z_h was binned every 1 dBZ within the range of 5–60 dBZ. The frequencies in the CFADs were normalized to the maximum absolute frequency in each diagram to facilitate vertical comparisons (Houze et al. 2007).

We analyzed the atmospheric conditions of the Muroto Lines using observational and reanalysis data. Data from the JMA Automated Meteorological Data Acquisition System (AMeDAS) at Murotomisaki (blue triangle in Fig. 1c, the same location as the JMA Murotomisaki radar) and Kaiyo (red square in Fig. 1c) were used to analyze the atmospheric environment near the surface. The observation heights above the sea level at Murotomisaki and Kaiyo were 185 m and 5 m, respectively. We used local pressure, temperature, relative humidity (RH), and wind data from Murotomisaki and temperature data from Kaiyo at 10 min intervals. Vertical profiles of the 10 min averaged horizontal wind collected by the JMA wind profiler radar located in Kochi (green circle in Fig. 1c) were also used. We excluded data above 6 km in height owing to the high frequency of missing values. To analyze the thermodynamic environment, we used the initial value of the JMA Mesoscale model (JMA-MSM), provided every 3 hours. This dataset contained geopotential height, temperature, horizontal wind, and RH with a horizontal resolution of 0.125° (zonal) × 0.1° (meridional) and 16 pressure levels (10 levels for RH). We verified that the JMA-MSM data are valid for analyzing the thermodynamic environment of the Muroto Lines (see appendix A). The JMA surface weather charts were used to determine the synoptic environment.

3. Cases overview

Figure 3 shows the horizontal distribution of hourly rainfall during Case 1 derived from the XRAIN rainfall intensity. We analyzed the hourly rainfall field to capture the maintenance location of the Muroto Line. A line-shaped heavy rain area, where the hourly rainfall was 20 mm or greater with maximum rainfall exceeding 50 mm brought by the Muroto Line, clearly appeared between 12 and 20 JST on July 3, 2018. We primarily focused on this period when the Muroto Line clearly appeared. The Muroto Line persisted in almost the same area from 12 to 15 JST, then gradually shifted eastward between 15 and 17 JST, and was maintained at 5 km east after 17 JST. This shift resulted in the appearance of two lines of accumulated rainfall (Fig. 1c). We further divided Case 1 into Case 1A (12–15 JST) and Case 1B (17–20 JST) to compare the maintenance mechanisms between the two periods. The Muroto Line persisted until approximately 00 JST on July 4; however, its intensity was weak (not shown). Fig. 3

In Case 2, the Muroto Line produced intense rainfall from 16 to 21 JST on August 15, 2018 (Fig. 4). The Muroto Line persisted at almost the same location for 5 hours. The maximum hourly rainfall (127 mm, 19–20 JST) in Case 2 was slightly higher than that of Case 1 (107 mm, 16–17 JST). The Muroto Line occasionally appeared until 00 JST on August 16 but did not persist for longer than an hour (not shown). Fig. 4

4. Results

4.1 Atmospheric environments

Figures 5a and 5b show the JMA surface weather charts analyzed just before the Muroto Lines occurrences in two cases. In Case 1 (Fig. 5a), Typhoon Prapiroon was located 600 km west of the Muroto Line, and the North Pacific High existed to the east of Shikoku at 09 JST on July 3, 2018. The typhoon moved northeast at a speed of 25 km h^{-1} and reached east of Tsushima Island at 21 JST on July 3. The synoptic environment in Case 2 (Fig. 5b) was similar to that in Case 1, as characterized by two tropical cyclones (a tropical depression (TD in Fig. 5b) and typhoon Rumbia) to the west and the North Pacific High to the east of Shikoku. Although the typhoon Rumbia moved northwest at 21 JST on 15 August, the synoptic field remained mostly unchanged (not shown). Fig. 5

Figures 5c and 5d show the horizontal distributions of the equivalent potential temperature (EPT: calculated with a method of Bolton (1980)) and horizontal wind at the 950 hPa level, and geopotential height at the 500 hPa level derived from the initial value of the JMA-MSM at the same time as Figs. 5a and 5b, respectively. In Case 1, a warm-moist southeasterly airflow with an EPT higher than 345 K intruded into the eastern part of Shikoku at the 950 hPa level. Such a warm-moist airflow also flowed into the area from south-southeast in Case 2. The 5880 m contour line of the geopotential height at the 500 hPa level in Case 2 extended farther west than in Case 1, indicating that the North Pacific High was stronger in Case 2. The absence of an upper-level trough, the strong low-level convergence ($>2.0\times10^{-4}$) not related to the surface roughness near Shikoku (Figs. 5c and 5d), and the distant location (800 km north of Shikoku) of the stationary fronts (Figs. 5a and 5b) suggest that synoptic forced convergence should not play a direct role in the maintenance of the Muroto Lines.

Figure 6 shows the skew-T log-p diagrams of temperature and dew-point temperature (Fig. 6a) and vertical profiles of RH (Fig. 6b) at 12 JST on July 3, 2018 (Case 1, solid lines) and at 15 JST on August 15, 2018 (Case 2, dashed lines). Each profile is the mean value averaged within a red dashed rectangle (0.325°x0.3°), as shown in the lower-left map of Fig. 6a, corresponding to the upstream side of the low-level wind of the Muroto Line in both cases. The vertical temperature profiles in both cases indicate a conditionally unstable environment. The convective available potential energy (CAPE), convective inhibition (CIN), lifted condensation level (LCL), LFC, and level of neutral buoyancy (LNB) in Case 1 (Case 2), averaged over the same areas as the profiles in Fig. 6, were 810 J kg^{-1} (2111 J kg^{-1}), 0.0 J kg^{-1} (0.2 J kg^{-1}), 518 m (544 m), 618 m (1252 m), and 11673 m (14786 m), respectively. The lower LFC and almost zero CIN values suggest that convective cells can be easily triggered by upslope lifting over small-scale ridges on the Muroto Peninsula (Fig. 1b). The higher values of CAPE and LNB in Case 2 indicate that the atmospheric conditions were more favorable for deeper convection than in Case 1, which is consistent with the vertical cross-sections of the Muroto Lines (Fig. 2). The RH (Fig. 6b) exceeded 75% below the 600 hPa level in both cases, indicating a moist environment below the middle troposphere.

Fig. 6

Fig.7

Figure 7 shows the time series of the AMeDAS observations at Murotomisaki and Kaiyo (only shown at the potential temperature). The potential temperature was displayed because the observation heights of the two sites differed by 180 m. The sea level pressure at Murotomisaki was used to calculate the potential temperature at Kaiyo. In Case 1, the surface wind speed was maintained between 12 and 15 m s^{-1} (Fig. 7a). The wind speed of Case 2 (Fig. 7f) was weaker (5–9 m s^{-1}) than that of Case 1. The surface wind direction in Case 1 (Fig. 7b) gradually shifted from east-southeasterly at 12 JST to south-southeasterly at 20 JST. The Muroto Line occurred when the wind direction was between south-southeasterly and east-southeasterly. From 14:10 to 17:10 JST, the wind direction changed from east-southeasterly to south-southeasterly, almost coinciding with the transition from Case 1A to Case 1B. This suggests that the transition in the maintenance location of the Muroto Line could be linked to veering of the surface wind direction, which could be caused by the northeastward movement of the typhoon (Fig. 5a). Case 2 occurred when the wind direction ranged between south-southeasterly and southeasterly (Fig. 7g). The amount of surface water vapor flux (WVF: defined by WVF = $\rho\, q_v\, u$, where ρ is air density, q_v is water vapor mixing ratio, and u is wind speed) was higher (250–350 g m^{-2} s^{-1} in Case 1 and 190–250 g m^{-2} s^{-1} in Case 2) than the value of favorable atmospheric conditions for QSCBs presented by Kato (2020) (>150 g m^{-2} s^{-1}) in both cases, indicating the rich intrusion of water vapor to the Muroto Lines. The temporal changes in the amount of WVF were explained by the wind speed in both cases, as the water vapor mixing ratio remained almost constant

(Figs. 7c and 7h). The potential temperatures at Murotomisaki and Kaiyo (solid and dashed lines in Figs. 7e and 7j, respectively) showed that the differences between the two sites were within 2 K, and no steep temperature drop was observed at Kaiyo (5 km east of the Muroto Line). This implies that the strong cold outflow induced by the Muroto Line could not reach Kaiyo.

Figure 8 shows hodographs of the mean horizontal wind below a height of 6 km obtained by the wind profiler radar at Kochi and the AMeDAS at Murotomisaki during each period. All cases were characterized by veering features in the wind direction. The values of SREH (calculated from the surface to 3 km in height and cell-motion speed was estimated with a method of Bunkers et al. (2000)) during Case 1A, 1B, and 2 were 213.7 m^2 s^{-2}, 194.5 m^2 s^{-2}, and 83.0 m^2 s^{-2}, respectively, suggesting the existence of strong vertical wind shear. The orientations of the Muroto Line, obtained by averaging those of the heavy rain areas (Figs. 3 and 4), almost corresponded to the direction of the southerly wind between 2 and 4 km in height in all periods. From Case 1A to Case 1B (Figs. 8a and b), the lowest-level (below 600 m in height) wind direction transitioned from between east-southeasterly and southeasterly to south-southeasterly. The vertical profile of the horizontal wind direction in Case 2 (Fig. 8c) was similar to that in Case 1B; however, the wind speed in Case 2 was half of that in Case 1B below 6 km in height.

Fig. 8

4.2 Horizontal structures of the Muroto Lines

Figure 9 shows a time-latitude section of XRAIN maximum rainfall intensity between 134.1°E and 134.4°E during Case 1 to clarify the meridional movement of convective cells. Maximum rainfall intensity frequently reached stronger than 120 mm h^{-1} between 33.65°N and 33.80°N, and occasionally exceeded 150 mm h^{-1}. Many lines of strong rainfall intensity extending diagonally up to the right appeared in this case. This indicates that convective cells were generated in the southernmost part of the Muroto Line (mostly between 33.4°N and 33.5°N) and moved northward, suggesting that the Muroto Line in Case 1 was a BB type QSCB. The meridional moving speed of convective cells estimated from the orientation of lines of heavy rainfall (indicated by dashed-arrows in Fig. 9) was between 20 and 25 m s^{-1}, almost corresponding to the southerly component of wind speed at approximately 2–4 km in height (Figs. 8a and 8b). The southernmost tip of the strong rainfall intensity (greater than 20 mm h^{-1}) shifted approximately 5 km north after 17 JST.

Fig. 9

Figure 10 shows the time-latitude section of XRAIN maximum rainfall intensity between 134.15°E and 134.45°E during Case 2. Maximum rainfall intensity usually exceeded 120 mm h^{-1} between 33.55°N and 33.75°N. Convective cells were continuously generated until 20 JST from 33.4°N, and the northward advection speed estimated from the dashed arrows in Fig. 10 was between 10 and 15 m s^{-1}. This suggests that the Muroto Line in Case 2 was a BB-type QSCB, similar to Case 1. The meridional moving speed mostly corresponded to the meridional component of wind speeds higher than 2 km in height (Fig. 8c).

Fig. 10

Figure 11 shows longitude-time cross sections of XRAIN rainfall intensity around the southernmost part of the Muroto Lines to capture their temporal variations of zonal distribution. In Case 1 (Fig. 11a), convective cells of the Muroto Line passed around 134.18°E until 15 JST (i.e., during Case 1A). The locations of convective cells gradually shifted to the east after 15 JST and maintained around 134.22°E after 17 JST. In Case 1B, weak convective cells repeatedly appeared at the location where Case 1A was maintained, indicating the existence of a weak convection on the west of the Muroto Line. A weak band due to the weak convection appeared between 17 and 20 JST (Fig. 3). A similar weak convection persisted 5 km west of the Muroto Line in Case 2 (Fig. 11b). This led to the formation of a slightly bulged area of weak hourly rainfall west of the Muroto Line between 33.4°N and 33.55°N (Fig. 4). Results from Fig. 11 indicate that convective cells were simultaneously generated at two locations during Case 1B and Case 2, and those appeared on the upwind (i.e., eastern) side of the low-level wind developed into the Muroto Line. Fig. 11

To clarify the relationship between the maintenance location of the Muroto Lines and orography, we compare the mean XRAIN rainfall intensity with orography (Fig. 12). In Case 1A (Fig. 12a), the Muroto Line was maintained over the SN Main Ridge, and the southernmost tip of the Muroto Line (mean rainfall intensity greater than 1 mm h^{-1}) was located over the SR (Fig. 12b). The Muroto Line brought the strongest rainfall around 33.72°N, 133.21°E, where relatively high orography (higher than 1000 m in height) was located. A small peak in the mean rainfall intensity greater than 30 mm h^{-1} was also found Fig. 12

around 33.5°N, just north of the CV1. During Case 1B (Fig. 12c), the Muroto Line was maintained 5 km east of Case 1A. The southernmost tip of the Muroto Line shifted toward the eastern foot of the SR (Fig. 12d). The orography beneath the southern part of Muroto Line is generally lower than 500 m in height. The strongest rainfall (a contour higher than 50 mm h^{-1}) appeared around the southernmost slope of the Shikoku Main Ridge. A small peak in mean rainfall intensity appeared just north of the CV2. The weak convection shown in Fig. 11a is located west of the Muroto Line (Figs. 12c and 12d). In Case 2, the Muroto Line was maintained at almost the same location as that in Case 1B, and its southernmost tip was located over the eastern foot of the SR (Fig. 12f). The contour of 1 mm h^{-1} bulged to the west between 33.4°N and 33.55°N indicates the weak convection shown in Fig. 11b. These suggest that the convective cells of the Muroto Lines were not always generated over the ridges located beneath the southernmost part of the Muroto Lines.

4.3 Vertical structures of the Muroto Lines

Figure 13 displays the appearance frequencies of the longitudinal maximum echo-top height obtained from the JMA Murotomisaki radar. The longitudinal maximum values were obtained in the areas surrounded by red-dotted rectangles in Fig. 12 for each period. The longitudinal maximum mean rainfall intensity obtained from the XRAIN rainfall intensity in the same area is also shown by black curve lines in Fig. 13. We analyzed the echo-top heights of 15 and 35 dBZ to capture the maximum height of rain and snow and the

Fig. 13

existence of heavy rain and graupel, respectively. In all periods, a high frequency (> 30%) appeared at each latitude, indicating that the developmental stages of each convective cell at a certain latitude were generally the same. This allowed us to statistically capture the general characteristics of the vertical structures of Muroto Line at that latitude. In analyzing the vertical structures, we divided the Muroto Line into three stages along latitude based on the representative developmental stage of convective cells, as shown in Fig. 13: The developing stage (the highest frequency of 15 dBZ echo-top heights increase toward the north), the mature stage (the 15 dBZ echo-top heights remain mostly constant and maximum mean rainfall intensity higher than 50 mm h^{-1}), and the dissipating stage (the 15 dBZ echo-top height decreases toward the north). In this study we mainly focus on the developing and mature stages. During Case 1A, the 15 dBZ echo-top height (Fig. 13a) was mostly lower than 9 km in height and most of the 35 dBZ echo-top height (Fig. 13b) did not exceed the -10°C level. The highest value of maximum mean rainfall intensity appeared at 33.72°N, where a high 15 dBZ echo-top height (9 km) frequently observed, suggesting that the mature stage of convective cells brought the strongest rainfall. A small peak in maximum mean rainfall intensity also appeared at 33.49°N, corresponding to the small peak of mean rainfall intensity found in Fig. 12b. The peak in maximum mean rainfall intensity appearing at 33.84°N is doubtful because it is located near the XRAIN C-band radar, where erroneous data frequently appear, as described in Section 2. The echo-top height in Case 1B (Figs. 13c and 13d) had characteristics similar to those of Case 1A. The differences of maximum mean rainfall intensity can be found between 33.73°N and 33.76°N, where the intensity rapidly increased at the south of its highest value. The location of this rapid increase corresponds to the southern slope of the Shikoku Main Ridge, implying that upslope lifting further developed the Muroto Line. In both periods, mean maximum rainfall intensity greater than 20 mm h^{-1} appeared at the developing stage of convective cells where the peak appearance frequency of 15 dBZ echo-top height existed around the 0°C level (around 33.5°N). In Case 2, the 15 dBZ echo-top height exceeded 16 km at a maximum (Fig. 13e) and high appearance frequency of 35 dBZ echo-top height usually reached higher than the -10°C level (Fig. 13f), suggesting the existence of ice particles. The location of the highest mean maximum rainfall intensity and the highest 15 dBZ echo-top height matched, suggesting that the most intense rainfall occurred at the mature stage of the convective cells. The high maximum rainfall intensity also appeared at the developing stage of convective cells as in Case 1.

Figure 14 shows the two cases (Case 1B and Case 2) of normalized CFADs analyzed Fig. 14 over the areas indicated by black dashed rectangles in Fig. 12: the southernmost part of the intense rainfall area (mean rainfall intensity of 20 mm^{-1} or greater) and the strongest rainfall area. The number of samples collected at each height is shown in the right panel of each CFAD. Case 1A was excluded from the CFAD analysis because of the appearance of severe beam blockage where the Muroto Line maintained. In the strongest rainfall area of Case 1B (Fig. 14a), the value of median Z_h was 15 dBZ at the -10°C level (6.7 km in height) and rapidly increased to 29 dBZ at the 0°C level (4.8 km in height), then reached 40 dBZ at 1.5 km in height. This suggests that Z_h growth below the 0°C level was essential for producing intense rainfall in Case 1B. In the strongest rainfall area of Case 2 (Fig. 14c), the median values of Z_h at the -10°C level, the 0°C level (5.2 km in height), and at 1.5 km in height were 30 dBZ, 37 dBZ, and 44 dBZ, respectively. The number of samples collected at each height (the right panel of Fig. 12c) was almost constant below 12 km. Compared with Case 1B, the vertical structure of Case 2 was characterized by a high Z_h above the 0°C level and a lower Z_h growth below that level. These suggest that melting of ice particles was the primary factor in producing the strongest rainfall in Case 2.

The vertical Z_h structure between the two cases in the southernmost part of the heavy rainfall area (Fig. 14b and 14d) differed from that in the strongest rainfall area, particularly in Case 2. In Case 1B (Fig. 14b), the vertical profile of median value of Z_h was similar (15 dBZ at the -10°C level, 26 dBZ at the 0°C level, and 40 dBZ at 1.5 km in height) to that in the strongest rainfall area. While the number of samples (the right panel of Fig. 14b) rapidly decreased above the 0°C level, indicating that intense rain at the southernmost part of intense rainfall area brought by shallower rainfall than that of the strongest rainfall area in Case 1B. In Case 2 (Fig. 14d), the median values of Z_h above 0°C was lower than that in the strongest rainfall area (22 dBZ at the -10°C level and 31 dBZ at 0°C) but increased to 43 dBZ at 1.5 km in height. Such a lower Z_h above the 0°C level and a large Z_h growth below that level resemble those observed in Case 1B. These results suggest that the Z_h

growth below the 0°C level was important to produce intense rainfall in the southernmost part of the heavy rainfall area in both cases, where convective cells were developing.

5. Discussion

5.1 Maintenance mechanisms of the Muroto Lines

In both cases, the Muroto Lines suggested BB-type QSCBs with a line-shaped structure sustained through successive generation of convective cells in the southernmost part of the Muroto Lines and their northward advection. The atmospheric environmental factors affecting the maintenance of the Muroto Lines were as follows: (1) Intrusion of warm-moist air with a high EPT (greater than 345 K) from east-southeast and south-southeast at the lowest level. The inflow was conditionally unstable with almost zero CIN, a moderate to high CAPE value (810 J kg^{-1} in Case 1 and 2111 J kg^{-1} in Case 2), an LFC of approximately 1000 m or lower, and a large amount of WVF. Such airflow can easily trigger convective cells if weak forcing (i.e., orographic forcing) exists. (2) Southerly wind at 2−4 km in height. Convective cells were advected northward by the middle-level winds. This southerly wind formed a strong vertical wind shear with low-level winds, which were essential for forming QSCBs (e.g., Unuma and Takemi 2016b; Bluestein and Jain 1985; LeMone et al 1998). (3) Very high humidity (RH > 80%) below 0°C level (Fig. 6). This can suppress the evaporative cooling of raindrops and lead to weak storm-generated cold outflow induced by the Muroto Line, which are usually important for the maintenance of BB-type QSCBs (Schumacher and Johnson 2005). The absence of a strong cold outflow is evident from the lack of a steep temperature decrease near the Muroto Line (Figs. 7e and 7j). As the Muroto Lines were maintained over mountainous areas without synoptic low-level convergence (Fig. 5), orography should have played an essential role in their maintenance instead of the cold outflow. The stationarity of the Muroto Line also suggests a weak cold outflow. This is because, if a strong cold outflow exists, convective cells can be generated east of the Muroto Line, where the outflow and low-level inflow converge. The atmospheric conditions, excluding synoptic ascent (which was impossible to obtain from the data used in this study), met the favorable conditions suggested by Kato (2020), except for the SREH in Case 2 (83 $m^2 s^{-2}$). However, the veering wind structure enabled the maintenance of the BB mechanism.

Umemoto et al. (2005) suggested that convective cells of the Muroto Line were repeatedly generated by upslope lifting over mountains on the Muroto Peninsula. The results in Fig. 12 suggest that upslope lifting over ridge slopes can contribute to the maintenance of the Muroto Line in Case 1A. However, upslope lifting alone could not explain the cell generation mechanisms in Cases 1B and 2, where precipitation occurred at the eastern foot of the SR (Fig. 12). To address this issue, we calculated the unsaturated moist Froude number (Fr_w) for the SR which defined by $Fr_w = U / (N_w H)$; where H is the representative height of SR (750 m, corresponding to the maximum height of the SR), U is the mean horizontal speed below H obtained from Fig. 8, N_w is the unsaturated moist Brunt–Väisälä frequency defined by $N_w^2 = (g/\overline{\theta}_v)(\mathrm{d}\theta_v/\mathrm{d}z)$ (Emanuel 1994), where $\overline{\theta}_v$ (calculated from Fig. 6) is the mean virtual potential temperature below H, g is the acceleration of gravity, and $\mathrm{d}\theta_v/\mathrm{d}z$ is calculated by θ_v at H and the surface. Parameters to compute N_w are obtained from Fig. 6. The Fr_w values for Cases 1A, 1B, and 2 were 2.43, 2.64, and 1.20, respectively. For an idealized situation,

Fr_w greater than unity indicates that the flow passes over the mountain (e.g., Smith 1989; Smith 2019). This suggests that upslope lifting at the SR contributes to the formation of the southernmost convective cells in the Muroto Line, which cannot explain the eastern foot maintenance during Cases 1B and 2.

Instead of Fr_w, the relationship between the orientation of the SR and the lowest-level wind direction may explain the maintenance mechanisms of the Muroto Line. In Case 1A, the lowest-level wind was east-southeasterly (Fig. 8a), almost perpendicular to the SR orientation (from south-southwest to north-northeast). In contrast, the wind directions in Cases 1B and 2 were maintained when the lowest-level wind direction was southeasterly or south-southeasterly (Figs. 8b and 8c). The angle between the wind direction and the orientation of the SR in Case 1B was smaller than that in Case 1A. In a three-dimensional ridge, a flow with a lower angle of incidence tends to disperse to both sides of the ridge because it impinges on the narrower side of the ridge (Smith 1989). In addition, partial flow splitting, in which both upslope lifting and flow splitting occur simultaneously, has been reported in numerical simulations for both ideal (Smolarkiewicz and Rotunno 1989) and real orography (Yu et al. 2022) even when $Fr > 1$ (i.e., $Fr_w > 1$). Considering the lower angle of incidence of the lowest-level wind and the appearance of the weak convection over the SR (Figs. 11, 12d, and 12f), partial flow splitting could have occurred during Cases 1B and 2 at the southern slope of the SR. When this occurred, two bands could be formed: the first was formed by upslope lifting, and the second was generated by low-level convergence at the eastern foot of the SR, which could be created by the split flow deflected to the south-southwesterly and undeflected southeasterly or south-southeasterly flow. In this case, the band formed at the eastern foot of the ridge (i.e., the Muroto Line) could have developed because this band was formed on the upstream side of the warm-moist lowest-level wind intruding from southeasterly and south-southeasterly. However, the band formed over the ridge could not develop further because the Muroto Line disrupted the supply of low-level water vapor, resulting in the formation of a weak convection (Fig. 11).

The Muroto Lines could be further developed by acquiring water vapor from the lateral side of the Muroto Line because the low-level wind direction was not parallel to the orientation of the Muroto Line. Seko and Nakamura (2003) showed that a cross-QSCB low-level flow can form a BSB-type QSCB. However, the weak outflow from the Muroto Line can create unfavorable conditions for the lateral triggering of convective cells, resulting in the formation of the BB-type Muroto Line. The importance of lateral inflow is also suggested by the weakening of the Muroto Line after 20 JST in Case 1 (Fig. 3), despite the increase in WVF (Fig. 7d). This weakening may have occurred because of a decrease in the eastern component of the low-level wind (Fig. 7b), resulting in a reduction in the lateral intrusion of water vapor.

Small-scale orographic features beneath the Muroto Line may contribute to its further development. In Case 1A (Case 1B), the mean rainfall intensity had a small peak immediately north of CV1 (CV2) (Fig. 12b and 12d). CV1 and CV2 are concave valleys opening on the east-southeast side and the south-southeast sides, respectively, corresponding to the low-level wind direction in each case. These situations favor the convergence of low-level water vapor in concave valleys (Morotomi et al. 2012; Yu et al. 2022), resulting in a sufficient supply of water vapor to the Muroto Line.

This study suggests that orographic effects on small-scale topography beneath and near the Muroto Line and the lateral intrusion of low-level water vapor play key roles in Muroto Line maintenance. These factors could prevail under warm-moist environment, which is unfavorable for the formation of a strong cold outflow.

5.2 Vertical structures and heavy-rain-producing processes of the Muroto Line

The vertical structures of Z_h (Figs. 13 and 14) indicate that convective cells of the Muroto Line in Case 1 were relatively shallow with a 15 dBZ echo-top height mostly below 9 km (Fig. 13a), whereas those in Case 2 were characterized by deep convections whose 15 dBZ echo top-height was higher than 16 km at maximum (Fig 13c). Most of the 35 dBZ echo-top heights appeared below the -10°C level in Case 1 (Figs. 13b and 13d), while that in Case 2 frequently appeared above the -10°C level (Fig. 13f). This suggests that graupel particles might be mostly absent in Case 1, whereas a sufficient number of graupel particles could be present in Case 2. Z_h from targets dominated by other solid particles (e.g., snow and ice crystals) are typically lower than 35 dBZ, while those dominated by graupel particles usually exceed 35 dBZ (Dolan et al. 2013; Kouketsu et al. 2015). These differences can be attributed to differences in atmospheric instability. The atmospheric environment in Case 1 was characterized by relatively low CAPE and LNB (810 J kg^{-1} and 11673 m, respectively) and high RH (>75%) below the middle level, featuring a relatively stable and humid environment, which is not favorable for deep moist convection. These characteristics are comparable to those of the Baiu (Meiyu) season in East Asia (Zhang et al. 2006), where heavy rainfall with relatively shallow convection is frequently observed (e.g., Zhang et al. 2006; Oue et al. 2010; Oue et al. 2011). In contrast, the CAPE and LNB values were high (2111 J kg^{-1} and 14786 m, respectively) in Case 2, corresponding to the atmospheric conditions of deep convective heavy rainfall (e.g., Bluestein and Jain 1985; Araki et al. 2021). The tendencies of the echo-top heights in Cases 1A and 1B were almost the same, suggesting that the differences in the vertical structures between the two periods were small.

The CFADs at the strongest rainfall area in the two cases (Figs. 14a and 14c) suggests that the strongest rainfall in Case 1B were produced by collision-coalescence of raindrops below the 0°C level, while those in Case 2 were primarily brought by the melting of graupel particles. In Case 1B (Fig. 14a), the vertical profile of the median of Z_h was characterized by the large decreasing rate of Z_h above the 0°C level (7.4 dBZ km^{-1} from the 0°C to the -10°C level) and lower appearance height of the peak value. These features correspond to the vertical profile of Z_h in the convection of medium depths described by Zhang et al. (2006), which are relatively shallow convective cells (echo-top height of 15 dBZ is 8 km or lower) frequently observed during the Baiu (Meiyu) season. In the convection of medium depths, the collision-coalescence of raindrops is usually a key factor in the production of heavy rainfall (Oue et al. 2010; Oue et al. 2011). The large increment of Z_h between the 0°C level and 1.5 km in height (from 29 dB to 40 dBZ in median Z_h) in Fig. 14a suggests that collision-coalescence of raindrops was also the primary factor in producing of the strongest rainfall in Case 1B. The collision-coalescence process is the primary microphysical process that causes the significant increase in Z_h with descending height below the melting layer (Kumjian and Prat 2014; Kumjian et al. 2022). We note that Z_h increased as height decreased by 2 km in Fig. 14a, well below the melting layer (typically within 1 km below the 0°C level, according to Shusse et al. 2011). A relatively stable and very humid environment and thick warm cloud layer (depth from LCL to the 0°C level; 3.8 km) in Case 1B also suggests a high efficiency for the collision-coalescence process, because raindrops could remain for a long time below the 0°C layer without evaporation. In Case 2 (Fig. 14c), the median value of Z_h at the 0°C level was very high (37 dBZ) and reached 30 dBZ even at the -10°C level, inferring the existence of sufficient number of graupel particles. We note that Z_h from graupel particles could become 30 dBZ (e.g., Yamada et al. 2004; Dolan et al. 2013). Although Z_h increased below the 0°C level, it suggests the occurrence of collision-coalescence of raindrops, with the magnitude of increment (7 dBZ from the 0 °C to 1.5 km in height in median values) being smaller than that in Case 1B (11 dBZ). This suggests that the melting of graupel particles was the primary factor producing the strongest rainfall in Case 2, a typical rain producing process in deep convective clouds. The unstable environment of Case 2 could have led to an efficient growth of graupel particles above the 0°C level, as strong updraft supplied a sufficient value of supercooled droplets and formed a favorable condition in the occurrence of riming process (Rutledge and Hobbs 1984; Deierling and Petersen 2008).

Strong rainfall (>20 mm h^{-1} in mean rainfall intensity) also occurred during the developing stage of convective cells in both cases (Fig. 13). This is different from the atypical scheme of convective cells in which intense rainfall is caused by the mature stage of convective storms (Byers and Braham 1949). The high growth rate of Z_h below 0°C level observed in both cases (Fig. 14b and 14d), indicated that collision-coalescence of raindrops was dominant regardless of the atmospheric instability. The valley convergence formed at CV2 may have contributed to the promotion of warm rain processes by supplying a large amount of water vapor to convective cells.

6. Summary

This study examines the maintenance mechanisms of Muroto Line, a south-north oriented QSCB that appeared from the Muroto Peninsula in eastern Shikoku, Japan. The analysis area is characterized by complex orography, where many small-scale ridges are embedded in larger-scale ridges. We focused on two cases of Muroto Lines with differing depth of convective clouds: Case 1 (12-20 JST on July 3, 2018) and Case 2 (16-21 JST on August 15, 2018). Figure 15 summarizes the maintenance and development mechanisms of the Fig. 15 Muroto Lines suggested in this study. In both cases, atmospheric environments were characterized by warm-moist and conditionally unstable lowest-level inflows between east-southeasterly and south-southeasterly, and high humidity below the middle troposphere. Both cases exhibited back-building structures; convective cells were continuously generated at the southernmost tip of the Muroto Lines and advected northward by southerly wind 2–4 km in height. However, the cell-generating mechanism in Case 1A differed from that in Case 1B and Case 2. In Case 1A (Fig. 15a), the lowest-level wind was east-southeasterly and the convective cells that generated over a small-scale ridge oriented from south-southwest to north-northeast (SR) could be caused by upslope lifting over the SR. In Case 1B and Case 2 (Figs. 15b and 15c), on the other hand, the lowest-level wind was southeasterly or south-southeasterly and the convective cells were generated at the east of the SR. This could be caused by convergence at the eastern foot of the ridge resulting from deflected flow at the ridge combined with undeflected flow. At the same time, part of the flow that encountered the SR was uplifted and formed weak convection over the SR. Convergence at small-scale concave valleys and the lowest-level inflow with easterly components could further develop the Muroto Line in both cases.

The vertical structures of the Muroto Lines showed that the strongest rainfall in Case 1 (Case 2) was primarily caused by relatively shallow (deep) convective cells, suggesting the importance of the collision-coalescence of raindrops (melting of graupel). In contrast, intense rainfall was also caused by the developing stage of convective cells by the collision-coalescence of raindrops in the southern part of the Muroto Lines.

This study suggests the importance of small-scale orographic effects and cross-QSCB lowest-level inflow for the maintenance of orographic QSCBs in warm-moist environments. To clarify the details of the wind field modulated by small-scale orography and cell-generating processes, numerical simulations with a horizontal resolution of 500 m or finer can be effective, as the horizontal scale of the small-scale orography focused on in this study was approximately 10 km. Furthermore, investigating the atmospheric environment and structures of other Muroto Line events can reveal the common conditions for the appearance of Muroto Lines and the relationship between the atmospheric environment and the depth of convective cells.

Appendix A

Comparison of the JMS-MSM data with sonde observations

To evaluate the validity of the JMA-MSM data used in this study, we compared it with upper-air soundings obtained around the periods when the Muroto Lines occurred (i.e., 09 and 21 JST on 3 July and 15 August in 2018). Sounding data obtained from four JMA sounding stations near the Muroto Line (Shionomisaki, Matsue, Fukuoka, and Kagoshima, shown in Fig. A1a) were used for comparison. We focused on temperature and RH, which Fig. A1 were used in this study, and compared these variables at the 925, 850, 700, 500, and 300 hPa levels. The JMA-MSM data were averaged within rectangles (0.375°×0.3°) that encompassed the sounding locations.

Results are shown in Figs. A1b and A1c. The JMA-MSM temperature closely matched with that of the soundings (Fig. A1b). A low root mean square error (RMSE; within 0.8 K) and a high correlation coefficient (CC; above 0.75) indicate a strong correlation between the two datasets. Similarly, the MSM RH also correlated with the soundings, with the CC above 0.75 and RMSE within 15%. Based on these results, we concluded that the JMA-MSM data are sufficiently accurate and valid for analyzing the thermodynamic environment of the Muroto Lines.

Data Availability Statement

XRAIN composite rainfall intensity data is available at the Data Integration and Analysis System (DIAS) operated by the Ministry of Education, Culture, Sports, Science and Technology of Japan (http://apps.diasjp.net/xband/). The initial value of JMA-MSM and the wind profiler radar data were provided by JMA and available from a data server operated by Research Institute for Sustainable Humanosphere (RISH), Kyoto University (http://database.rish.kyoto-u.ac.jp/index-e.html). AMeDAS data can be obtained at JMA website (https://www.data.jma.go.jp/stats/etrn/index.php). Digital Elevation Map provided by Geospatial Information Authority of Japan (https://fgd.gsi.go.jp/download/) (except for Fig. 1a) and National Aeronautics and Space Administration (NASA) Shuttle Radar Topography Mission (SRTM) 3 arc-seconds data (https://urs.earthdata.nasa.gov/) (for Fig. 1a) were used to display orography. Matplotlib (https://matplotlib.org) and Cartopy (https://scitools.org.uk/cartopy) were used for drawing figures. JMA Murotomisaki radar data is available from Japan Meteorological Business Support Center.

Acknowledgments

The authors sincerely thank the editor and two anonymous reviewers for their valuable and constructive comments. The authors also appreciate to Mr. M. Kato for the supporting of analyzing the JMA Murotomisaki radar data and Prof. K. Tsuboki, Dr. S. Kanada, and other members of the Laboratory of Meteorology, Institute for Space-Earth Environmental Research in Nagoya University for their fruitful comments. This work was performed using the facilities of the Institute for Space-Earth Environmental Research, Nagoya University. The work was also supported by "formation of a virtual laboratory for diagnosing the earth's climate system (VL)" defrayed by the MEXT, Japan.

References

Araki, K., T. Kato, Y. Hirockawa, and W. Mashiko, 2021: Characteristics of atmospheric environments of quasi-stationary convective bands in Kyushu, Japan during the July 2020 Heavy Rainfall Event. *SOLA*, **17**, 8–15.

Barrett, A. I., S. L. Gray, D. J. Kirshbaum, N. M. Roberts, D. M. Schultz, and J. G. Fairman Jr., 2015: Synoptic versus orographic control on stationary convective banding. *Quart. J. Roy. Meteor. Soc.*, **141**, 1101–1113.

Bluestein, H. B., and M. H. Jain, 1985: Formation of mesoscale lines of precipitation: Severe squall lines in Oklahoma during the Spring. *J. Atmos. Sci.*, **42**, 1711–1732.

Bolton, D., 1980: The computation of equivalent potential temperature. *Mon. Wea. Rev.*, **108**, 1046–1053.

Bunkers, M. J., B. A. Klimowski, J. Q. Zeitler, R. L. Thompson, M. L. Weisman, 2000: Predicting supercell motion using a new hodograph technique. *Wea. Forecasting*, **15**, 61–79.

Byers, H. R., and R. R. Braham Jr., 1949: *The thunderstorm.* U.S. Government Printing Office, 287pp.

Chappel, C. F., 1986: Quasi-stationary convective events. *Mesoscale Meteorology and Forecasting*, P. S. Rat, Ed., Amer. Meteor. Soc., 289–309.

Cressman, G. P., 1959: An operational objective analysis system. *Mon. Wea. Rev.*, **87**, 367–374.

Deierling, W., and W. A. Petersen, 2008: Total lightning activity as an indicator of updraft characteristics. *J. Geophys. Res.*, **113**, D16210, doi:10.1029/2007JD009598.

Dolan, B., S. A. Rutledge, S. Lim, V. Chandrasekar, and M. Thurai, 2013: A robust C-band hydrometeor identification algorithm and application to a long-term polarimetric radar dataset. *J. Appl. Meteor. Climatol.*, **52**, 2162–2186.

Doswell, C. A., H. E. Brooks, and R. A. Maddox, 1996: Flash flood forecasting: An ingredients-based methodology. *Wea. Forecasting*, **11**, 560–581.

Doviak, R., and D. Zrnić, 1992: *Doppler radar and weather observations. Second edition.* Academic Press, 562pp.

Emanuel, K. A., 1994: *Atmospheric Convection.* Oxford University Press, 580pp.

Gascón, E., S. Laviola, A. Merino, and M. M. Miglietta, 2016: Analysis of a localized flash-flood event over the central Mediterranean, *Atmos. Res.*, **182**, 256–268.

Hamada, A., and Y. N. Takayabu, 2018: Large-scale environmental conditions related to midsummer extreme rainfall events around Japan in the TRMM region. *J. Climate*, **31**, 6933–6945.

Hamada, A., Y. N. Takayabu, C. Liu, and E. J. Zipser, 2015: Weak linkage between the heaviest rainfall and tallest storms. *Nat. Commun.*, **6**, 6213, doi:10.1038/ncomms7213.

Hirockawa, Y., T. Kato, H. Tsuguti, and N. Seino, 2020: Identification and classification of heavy rainfall areas and their characteristic features in Japan. *J. Meteor. Soc. Japan*, **98**, 835–857.

Houze Jr., R. A., 2012: Orographic effects on precipitating clouds, *Rev. Geophys.*, **50**, RG1001, doi:10.1029/2011RG000365.

Houze Jr., R. A., D. C. Wilton, and B. F. Smull, 2007: Monsoon convection in the Himalayan region as seen by the TRMM Precipitation Radar. *Quart. J. Roy. Meteor. Soc.*, **133**, 1389–1411.

Kato, T., 1998: Numerical simulation of the band-shaped torrential rain observed over southern Kyushu, Japan on 1 August 1993. *J. Meteor. Soc. Japan*, **76**, 97–128.

Kato, T., 2005: Statistical study of band-shaped rainfall systems, the Koshikijima and Nagasaki Lines, observed around Kyushu Island, Japan. *J. Meteor. Soc. Japan*, **83**, 943–957.

Kato, T., 2020: Quasi-stationary band-shaped precipitation systems, named as "senjo-kousuitai", causing localized heavy rainfall in Japan. *J. Meteor. Soc. Japan*, **98**, 485–509.

Kato, T., and K. Aranami, 2005: Formation factors of 2004 Niigata-Fukushima and Fukui heavy rainfalls and problems in the predictions using a cloud-resolving model. *SOLA*, **1**, 1–4.

Kawano, T., and R. Kawamura, 2020: Genesis and maintenance processes of a quasi-stationary convective band that produced record-breaking precipitation in northern Kyushu, Japan on 5 July 2017. *J. Meteor. Soc. Japan*, **98**, 673–690.

Kouketsu, T., H. Uyeda, T. Ohigashi, M. Oue, H. Takeuchi, T. Shinoda, K. Tsuboki, M. Kubo, and K. Muramoto, 2015: A hydrometeor classification method for X-band polarimetric radar: Construction and validation focusing on solid hydrometeors under moist environments. *J. Atmos. Oceanic Technol.*, **32**, 2052–2074.

Kumjian, M. R., and O. P. Prat, 2014: The impact of raindrop collisional processes on the polarimetric radar variables. *J. Atmos. Sci.*, **71**, 3052–3067.

Kumjian, M. R., O. P. Prat, K. J. Reimel, M. van Lier-Walqui, and H. C. Morrison, 2022: Dual-polarization radar fingerprints of precipitation physics, a review. *Remote sens.*, **14**, 3706, doi:10.3390/rs14153706.

LeMone, M. A., E. J. Zipser, and S. B. Trier, 1998: The role of environmental shear and thermodynamic conditions in determining the structure and evolution of mesoscale convective systems during TOGA COARE. *J. Atmos. Sci.*, **55**, 3493–3518.

Morotomi, K., T. Shinoda, Y. Shusse, T. Kouketsu, T. Ohigashi, K. Tsuboki, H. Uyeda, and I. Tamagawa, 2012: Maintenance mechanisms of a precipitation band formed along the Ibuki-Suzuka mountains on September 2–3, 2008. *J. Meteor. Soc. Japan*, **90**, 737–753.

Ogura, Y., 1990: Analyses and mechanisms of intense precipitation. *Tenki*, **38**, 276–288 (in Japanese).

Oue, M., H. Uyeda, and Y. Shusse, 2010: Two types of precipitation particle distribution in convective cells accompanying a Baiu frontal rainband around Okinawa Island, Japan. *J. Geophys. Res.*, **115**, D02201, doi:10.1029/2009JD011957.

Oue, M., H. Uyeda, and D.-I. Lee, 2011: Raindrop size distribution parameters estimated from polarimetric radar variables in convective cells around Okinawa Island during the Baiu period. *Asia-Pac. J. Atmos. Sci.*, **47**, 33–44.

Oue, M., K. Inagaki, T. Shinoda, T. Ohigashi, T. Koketsu, M. Kato, K. Tsuboki, and H. Uyeda, 2014: Polarimetric Doppler radar analysis of organization of a stationary rainband with changing orientations in July 2010. *J. Meteor. Soc. Japan*, **92**, 457–481.

Pontrelli, M. D., G. Bryan, and J. M. Fritsch, 1999: The Madison County, Virginia, flash flood of 27 June 1995. *Wea. Forecasting*, **14**, 384–404.

Rutledge, S. A., and P. V. Hobbs, 1984: The mesoscale and microscale structure and organization of clouds and precipitation in midlatitude cyclones. XII: A diagnostic modeling study of precipitation development in narrow cold-frontal rainbands. *J. Atmos. Sci.*, **41**, 2949–2972.

Seko, H., and H. Nakamura, 2003: Numerical study of the shapes and maintenance mechanisms of meso-β scale line-shaped precipitation system in the middle-latitudes. *CAS/JSC WGNE Res. Activ. Atmos. Oceanic Modell.*, **33**, 5.30–5.31.

Shumacher, R. S., and R. H. Johnson, 2005: Organization and environmental properties of extreme-rain-producing mesoscale convective systems. *Mon. Wea. Rev.*, **133**, 961–976.

Shusse, Y., N. Takahashi, K. Nakagawa, S. Satoh, and T. Iguchi, 2011: Polarimetric radar observation of the melting layer in a convective rainfall system during the rainy season over the East China Sea. *J. Appl. Meteor. Climatol.*, **50**, 354–367.

Smith, R. B., 1989: Hydrostatic airflow over mountains. *Adv. Geophys.*, **31**, 1–41.

Smith, R. B., 2019: 100 years of progress on mountain meteorology research. *Meteor. Monogr.*, **59**, 20.1–20.73.

Smolarkiewicz, P. K., and R. Rotunno, 1989: Low Froude number flow past three-dimensional obstacles. part I: Baroclinically generated lee vortices., *J. Atmos. Sci.*, **46**, 1154–1164.

Sohn, B.-J., G.-H. Ryu, H.-J. Song, and M.-L. Ou, 2013: Characteristic features of warm-type rain producing heavy rainfall over the Korean Peninsula inferred from TRMM measurements. *Mon. Wea. Rev.*, **141**, 3873–3888.

Umemoto, Y., H. Hashiguchi, S. Fukao, and M. Teshiba, 2005: Wind variations around orographic rainband observed by wind profiler network in Japan. *Proc. of 11th Conference on Mesoscale Processes*, JP7J.7. [Available at https://ams.confex.com/ams/32Rad11Meso/webprogram/Paper97171.html.]

Unuma, T., and F. Murata, 2012: Statistical analysis of quasi-stationary line-shaped rainfall systems over Shikoku Island, Japan. *Tenki*, **59**, 119–125 (in Japanese).

Unuma, T., and T. Takemi, 2016a: Characteristics and environmental conditions of quasi‐stationary convective clusters during the warm season in Japan. *Quart. J. Roy. Meteor. Soc.*, **142**, 1232–1249.

Unuma, T., and T. Takemi, 2016b: A role of environmental shear on the organization mode of quasi-stationary convective clusters during the warm season in Japan. *SOLA*, **12**, 111–115.

Watanabe, H., and Y. Ogura, 1987: Effects of orographically forced upstream lifting on mesoscale heavy precipitation: A case study. *J. Atmos. Sci.*, **44**, 661–675.

Yamada, H., H. Uyeda, K. Kikuchi, M. Maki, and K. Iwanami, 2004: Dual-Doppler radar observations on factors causing differences in the structure of snow clouds during winter monsoon surges. *J. Meteor. Soc. Japan*, **82**, 179–206.

Yoshizaki, M., T. Kato, Y. Tanaka, H. Takayama, M. Tanaka, and Members of X-BAIU 98 observation, 2000: Analytical and numerical study of the 26 June 1998 orographic rainband observed in western Kyushu, Japan. *J. Meteor. Soc. Japan*, **78**, 835–856.

Yu, C.-K., and Y.-H. Hsieh, 2009: Formation of the convective lines off the mountainous coast of southeastern Taiwan: A case study of 3 January 2004. *Mon. Wea. Rev.*, **137**, 3072–3091.

Yu, C.-K., W.-F. Liu, L.-W. Cheng, and C.-Y. Lin, 2022: Mechanisms of valley precipitation enhancement over Da-Tun Mountain. *Mon. Wea. Rev.*, **150**, 1851–1871.

Yuter, S. E, and R. A. Houze Jr.,1995: Three-dimensional kinematic and microphysical evolution of Florida cumulonimbus. Part II: Frequency distributions of vertical velocity, reflectivity, and differential reflectivity. *Mon. Wea. Rev.*, **123**, 1941–1963.

Zhang, C. Z., H. Uyeda, H. Yamada, B. Geng, and Y. Ni, 2006: Characteristics of mesoscale convective systems over east part of continental China during the Meiyu from 2001 to 2003. *J. Meteor. Soc. Japan*, **84**, 763–782.

List of Figures

Fig. 1 (a) Location of Shikoku and orography [m] (shaded). The red-dashed rectangle indicates the area displayed in (b), while the blue-dashed rectangle denotes display areas of (c) and (d). (b) Distributions of orography (shaded) in the area surrounded by the red rectangle in (a). Areas enclosed by red-solid lines are the large-scale views of orography defined in this study (see text for details). A blue-dashed circle indicates the location of the Muroto Peninsula. Small-scale features in the Muroto Peninsula which will be described in this study are shown in a lower-right panel. Blue- and red-dotted lines show the locations of small-scale concave valleys (CV1 and CV2) and a ridge (SR), respectively. (c) Accumulated rainfall [mm $8h^{-1}$] observed by XRAIN from 12–20 JST on July 3, 2018 (colored contours) and the locations of observations. A red square, a blue triangle, and a green circle represent the locations of JMA AMeDAS at Kaiyo, JMA AMeDAS and JMA operational weather radar at Murotomisaki, and JMA wind profiler radar at Kochi, respectively. A yellow triangle represents the location of one of the XRAIN C-band polarimetric radars. (d) Same as (c), but accumulated rainfall [mm $5h^{-1}$] for 16–21 JST on August 15, 2018.

Fig. 2 Snapshots of horizontal reflectivity [dBZ] (Z_h) observed by JMA Murotomisaki radar. (a) A horizontal cross section at 2 km in height analyzed by Plan Position Indicator (PPI) scans observed from 17:33 to 17:38 JST on July 3, 2018. No-data areas are indicated by gray shading. (b) A vertical cross section along a dashed line shown in (a). (c) Same as (a), but from 17:43 to 17:48 JST on August 15, 2018. (d) Same as (b), but for along a dashed line shown in (c).

Fig. 3 Horizontal distributions of hourly rainfall [mm h^{-1}] derived from XRAIN between 11 and 21 JST on July 3, 2018. The maximum values of hourly rainfall for each period are displayed in the lower-right corner of each figure.

Fig. 4 Same as Fig. 3, but for between 15 and 22 JST on August 15, 2018.

Fig. 5 JMA surface weather charts analyzed at (a) 09 JST, on July 3, 2018, and (b) 15 JST on August 15, 2018. Red and blue crosses in (a) indicate the locations of typhoon at 15 and 21 JST on July 3, 2018, respectively. A red cross in (b) indicates the location of typhoon at 21 JST on August 15, 2018. (c) and (d) Horizontal distribution of equivalent potential temperature (EPT) [K] at the 950 hPa level (shaded), horizontal wind at the 950 hPa level (vectors), horizontal convergence stronger than 2.0×10^{-4} s^{-1} (white contours) at the 950 hPa level, and geopotential height at the 500 hPa level [m] (black contours) derived from the initial value of JMA-MSM on the same time as (a) and (b), respectively. The location of Shikoku is indicated by a red rectangle.

Fig. 6 (a) Skew-T log-p diagram collected from the initial value of JMA-MSM. Red and blue solid lines in (a) indicate vertical profiles of temperature [°C] and dew-point temperature [°C], respectively. Solid lines (dashed lines) represent the profile for 12 JST on July 3, 2018 (15 JST on August 15, 2018). Each value is a horizontal average within a red dashed rectangle (0.375°×0.3°) shown in the lower-left map. (b) Vertical profiles of relative humidity [%] obtained at the same time and location as (a). The solid and dashed lines have the same meanings as those in (a).

Fig. 7 Time series of (a) wind speed [m s^{-1}], (b) wind direction, (c) water vapor mixing ratio [g kg^{-1}], (d) water vapor flux (WVF) [g kg^{-1} s^{-1}], and (e) potential temperature [K] observed by JMA surface weather station at Murotomisaki (solid line) and Kaiyo (dashed line, only shown in potential temperature) from 09 to 24 JST on July 3, 2018. (f)–(j) Same as (a)–(e), but for from 13 to 24 JST on August 15, 2018. The gray-shaded periods represent times beyond the scope of this study. The locations of Murotomisaki and Kaiyo are shown in Fig. 1.

Fig. 8 Hodographs of horizontal wind [m s^{-1}] observed by JMA wind profiler radar at Kochi (circles) and JMA surface weather station at Murotomisaki (stars) averaged during (a) Case 1A (12 to 15 JST on July 3, 2018), (b) Case 1B (17 to 20 JST on July 3, 2018), and (c) Case 2 (16 to 21 JST on August 15, 2018). The colors of plots indicate the observation height (291 m intervals, except for the surface to the lowest wind profiler radar plot (109 m)). Red dashed lines indicate the orientation angles of the Muroto Lines obtained by averaging the orientations of hourly rainfall area 20 mm or grater during each period.

Fig. 9 Time-latitude section of maximum rainfall intensity [mm h^{-1}] between 134.1°E and 134.4°E obtained from XRAIN during Case 1 (from 12 JST to 20 JST on July 3, 2018). The orography in the analyzed area is shown on the left panel. The orientation of solid-arrows on the lower-right corner of figure indicates the representative meridional moving speed of convective cells. Dashed-arrows represent the meridional movement of several convective cells. A red-dashed line in the left panel indicates the latitude of a time-longitude cross section shown in Fig. 11a.

Fig. 10 Same as Fig. 9, but for maximum rainfall intensity [mm h^{-1}] between 134.15 °E and 134.45 °E during Case 2 (from 16 JST to 21 JST on August 15, 2018). A red-dashed line in the left panel indicates the latitude of a time-longitude cross section shown in Fig. 11a.

Fig. 11 Time-longitude cross section of XRAIN rainfall intensity [mm h^{-1}] (a) at 33.50°N during Case 1 (from 12 to 20 JST on July 3, 2018) and (b) at 33.45°N during Case 2 (from 16 to 21 JST on August 15, 2018). Black dashed circles indicate a weak convection formed west of the Muroto Line.

Fig. 12 Horizontal distribution of mean rainfall intensity [mm h^{-1}] (colored contour) derived from XRAIN and orography [m] (shaded) for (a) Case 1A (from 12 to 15 JST on July 3, 2018). A red-dashed rectangle indicates the displaying area of (b), (d), and (f). A red-dotted rectangle shows the analysis area of Fig. 13. (b) Enlarged display of (a) focusing on the southern part of the Muroto Line. Purple-dotted line displays the location of the SR small-scale ridge. Light- and dark-blue-dotted lines indicate locations of small-scale concave valleys named CV1 and CV2, respectively. (c) (d) Same as (a) and (b), respectively, but for Case 1B (from 17 to 20 JST on July 3, 2018). (e) (f) Same as (a) and (b), respectively, but for Case 2 (from 16 to 21 JST on August 15, 2018). Black-dashed rectangles and alphabets in (c) and (e) represent CFAD analyses areas and subcaptions in Fig. 14.

Fig. 13 Appearance frequency of the zonal maximum echo-top height obtained from JMA Murotomisaki CAPPI data [%] (shaded) and the zonal maximum value of mean XRAIN rainfall intensity [mm h^{-1}] (black solid curve lines). (a) (b) Maximum 15 dBZ and 35 dBZ echo-top height between 134.10°E and 134.25°E during Case 1A (from 12 to 15 JST on July 3, 2018), respectively. Solid, dashed, and dotted horizontal lines show the 0°C, -10°C, and -20°C height derived from Fig. 6, respectively. Red-dashed lines indicate boundaries between the developmental stages of typical convective cells of the Muroto Lines. The locations of SR and concave valleys (CV1 or CV2) beneath the Muroto Lines are indicated by brackets and arrows, respectively. (c) (d) Same as (a) and (b), respectively, but for the maximum values between 134.15°E and 134.40°E during Case 1B (from 17 to 20 JST on July 3, 2018). (e) (f) Same as (a) and (b), respectively, but for the maximum values between 134.15°E and 134.45°E during Case 2 (from 16 to 21 JST on August 15, 2018).

Fig. 14 Normalized Contoured Frequency by Altitude Diagrams (CFADs) of horizontal reflectivity (Zh) obtained from JMA Murotomisaki CAPPI data [%] sampled at (a) the strongest rainfall area, (b) the southernmost part of the intense rainfall area during Case 1B (from 17 to 20 JST on July 3, 2018). The analysis areas of each figure are displayed in Fig. 12. Bold solid curve lines indicate the vertical profile of the median of Zh. The thin solid, dashed, and dotted horizontal lines show the 0°C, -10°C, and -20°C levels derived from Fig. 6, respectively. The data below 1.5 km in height is masked by gray shade due to the lack of observation. The right panel of each figure shows the logarithmic number of samples at each height. (c), (d) Same as (a) and (b) respectively, but during Case 2 (from 16 to 21 JST on August 15, 2018).

Fig. 15 Schematic diagrams of the airflow structures and orography that contribute to the maintenance and development of the Muroto Lines suggested in this study. (a) Case 1A. The background shade indicates height of orography. The meanings of arrows, ellipses, and lines are shown in the legend (see text for the details of each element). (b) Same as (a), but for Case 1B. (c) same as (b), but for Case 2.

Fig. A1 (a) Locations of soundings stations used for the comparison with the JMA-MSM data. Circles and squares indicate the locations of sounding stations and averaging areas for the JMA-MSM (0.375°×0.3°), respectively. (b) Scatter plot comparing temperatures [K] from the soundings and the JMA-MSM data. The symbols represent data at different pressure levels: circle (925 hPa), inverted triangle (800 hPa), square (700 hPa), plus (500 hPa), and triangle (300 hPa). The colors correspond to the comparison locations: red (Shionomisaki), dark-blue (Matsue), light-blue (Fukuoka), and pink (Kagoshima). 'RMSE' and 'CC' in the legend denote root mean square error and correlation coefficient calculated for each level, respectively. (c) Same as (b), but for relative humidity [%].

Fig. 1

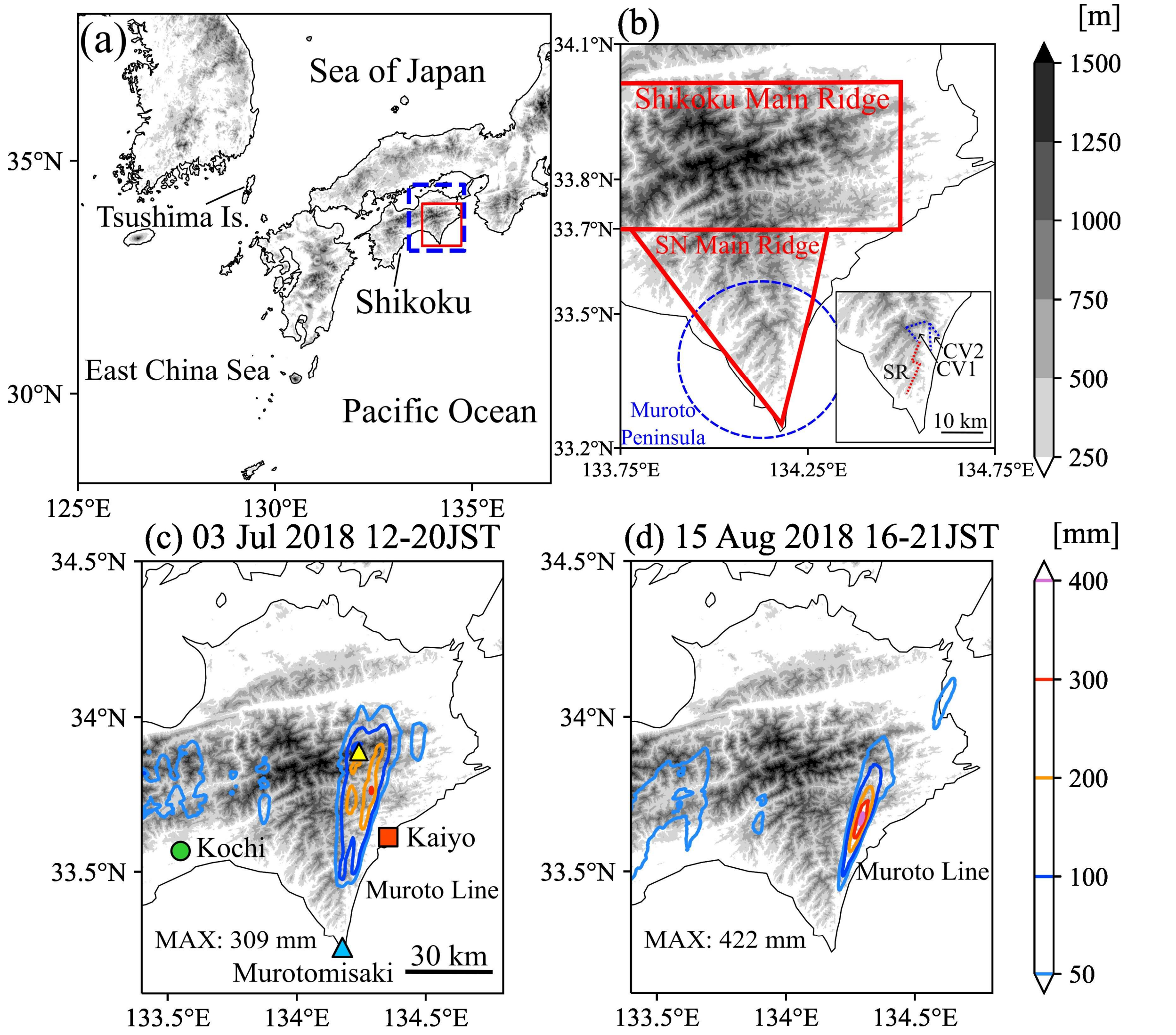

Fig. 1 (a) Location of Shikoku and orography [m] (shaded). The red-dashed rectangle indicates the area displayed in (b), while the blue-dashed rectangle denotes display areas of (c) and (d). (b) Distributions of orography (shaded) in the area surrounded by the red rectangle in (a). Areas enclosed by red-solid lines are the large-scale views of orography defined in this study (see text for details). A blue-dashed circle indicates the location of the Muroto Peninsula. Small-scale features in the Muroto Peninsula which will be described in this study are shown in a lower-right panel. Blue- and red-dotted lines show the locations of small-scale concave valleys (CV1 and CV2) and a ridge (SR), respectively. (c) Accumulated rainfall [mm $8h^{-1}$] observed by XRAIN from 12–20 JST on July 3, 2018 (colored contours) and the locations of observations. A red square, a blue triangle, and a green circle represent the locations of JMA AMeDAS at Kaiyo, JMA AMeDAS and JMA operational weather radar at Murotomisaki, and JMA wind profiler radar at Kochi, respectively. A yellow triangle represents the location of one of the XRAIN C-band polarimetric radars. (d) Same as (c), but accumulated rainfall [mm $5h^{-1}$] for 16–21 JST on August 15, 2018.

Fig. 2

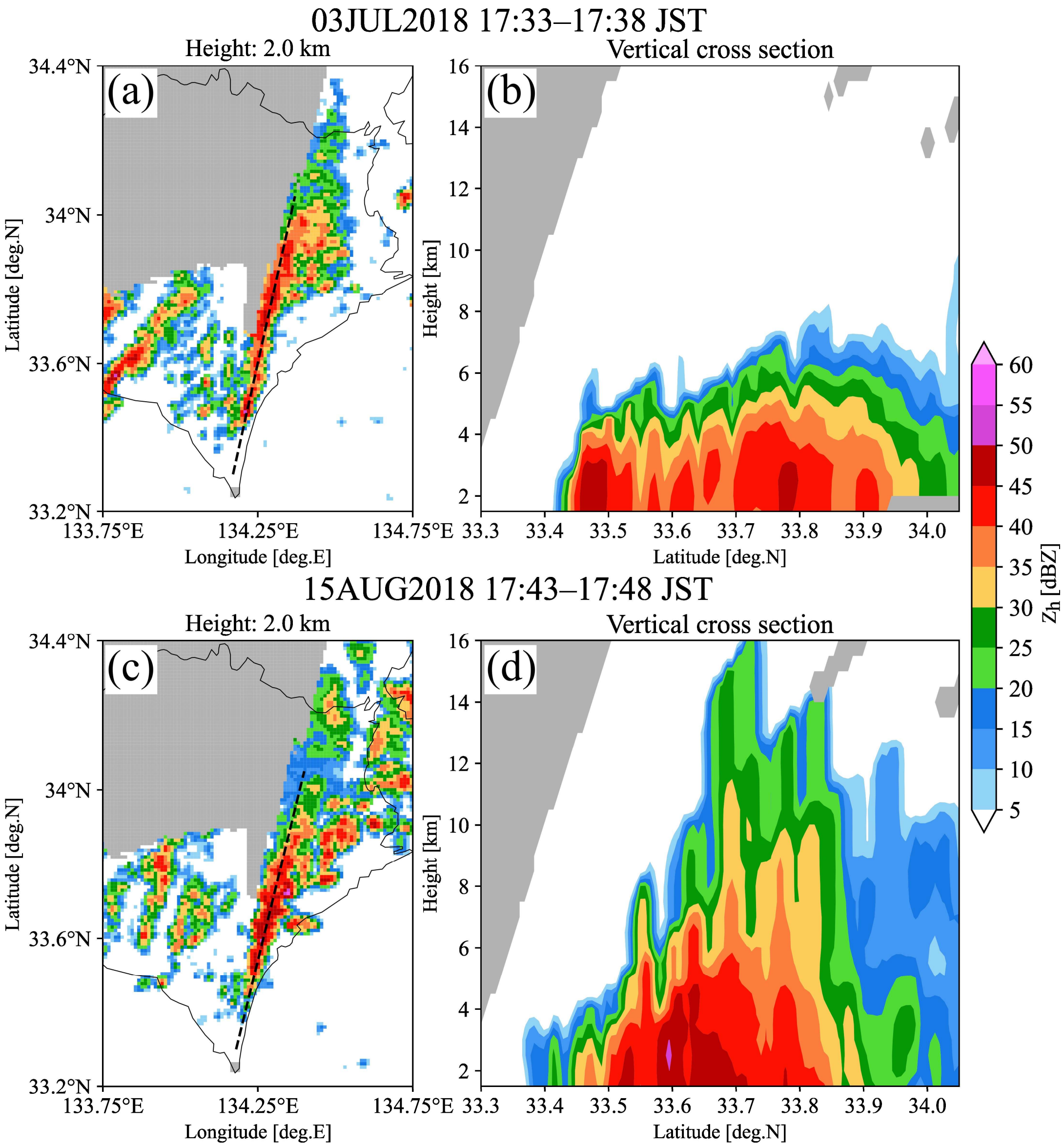

Fig. 2 Snapshots of horizontal reflectivity [dBZ] (Z_h) observed by JMA Murotomisaki radar. (a) A horizontal cross section at 2 km in height analyzed by Plan Position Indicator (PPI) scans observed from 17:33 to 17:38 JST on July 3, 2018. No-data areas are indicated by gray shading. (b) A vertical cross section along a dashed line shown in (a). (c) Same as (a), but from 17:43 to 17:48 JST on August 15, 2018. (d) Same as (b), but for along a dashed line shown in (c).

Fig. 3

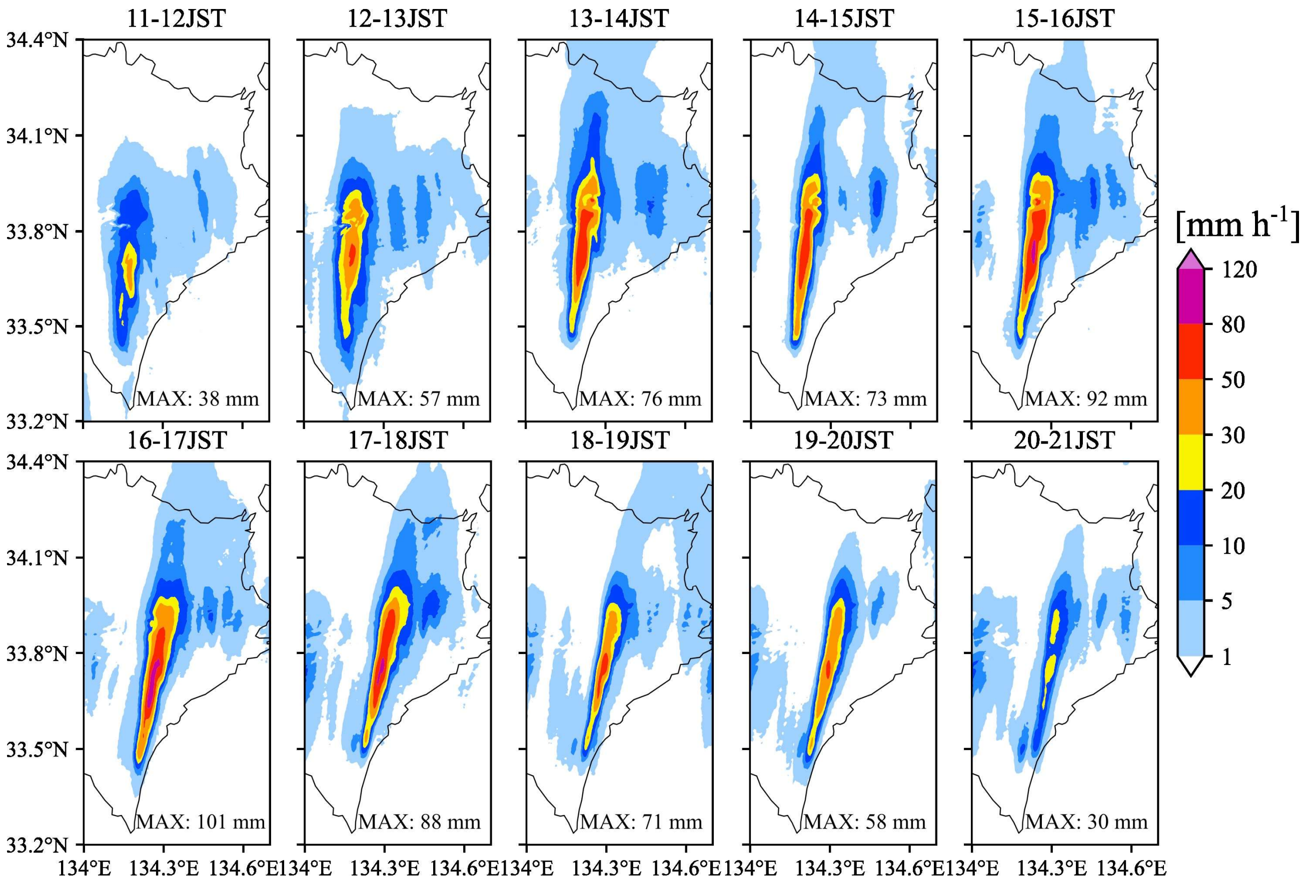

Fig. 3 Horizontal distributions of hourly rainfall [mm h^{-1}] derived from XRAIN between 11 and 21 JST on July 3, 2018. The maximum values of hourly rainfall for each period are displayed in the lower-right corner of each figure.

Fig. 4

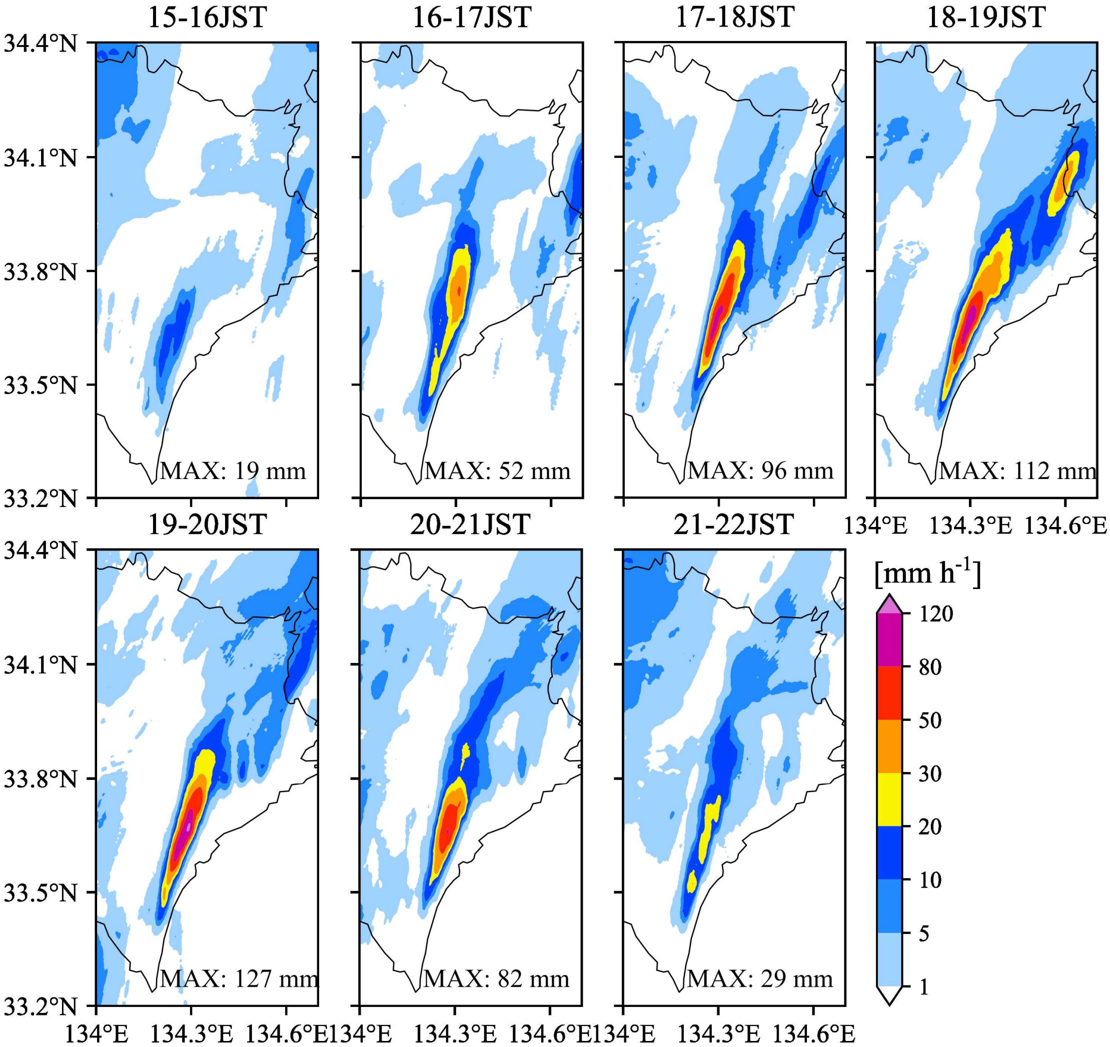

Fig. 4 Same as Fig. 3, but for between 15 and 22 JST on August 15, 2018.

Fig. 5

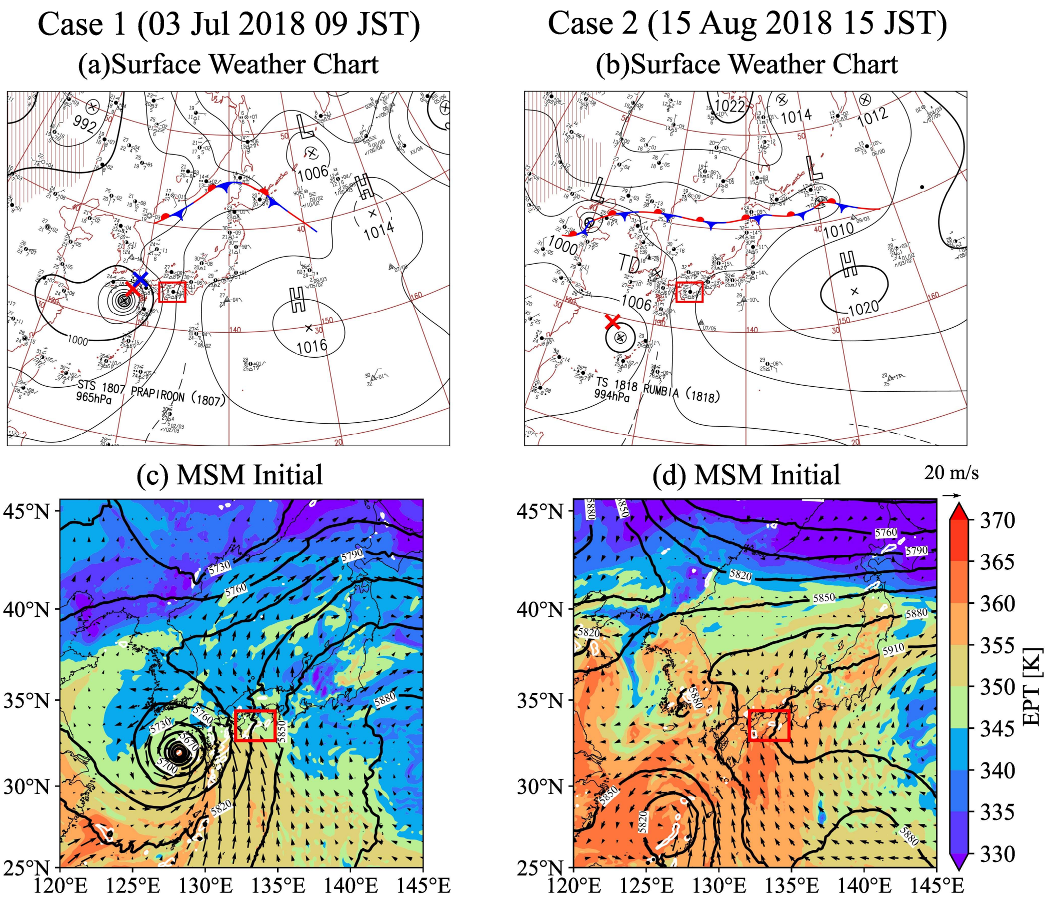

Fig. 5 JMA surface weather charts analyzed at (a) 09 JST, on July 3, 2018, and (b) 15 JST on August 15, 2018. Red and blue crosses in (a) indicate the locations of typhoon at 15 and 21 JST on July 3, 2018, respectively. A red cross in (b) indicates the location of typhoon at 21 JST on August 15, 2018. (c) and (d) Horizontal distribution of equivalent potential temperature (EPT) [K] at the 950 hPa level (shaded), horizontal wind at the 950 hPa level (vectors), horizontal convergence stronger than 2.0×10^{-4} s^{-1} (white contours) at the 950 hPa level, and geopotential height at the 500 hPa level [m] (black contours) derived from the initial value of JMA-MSM on the same time as (a) and (b), respectively. The location of Shikoku is indicated by a red rectangle.

Fig. 6

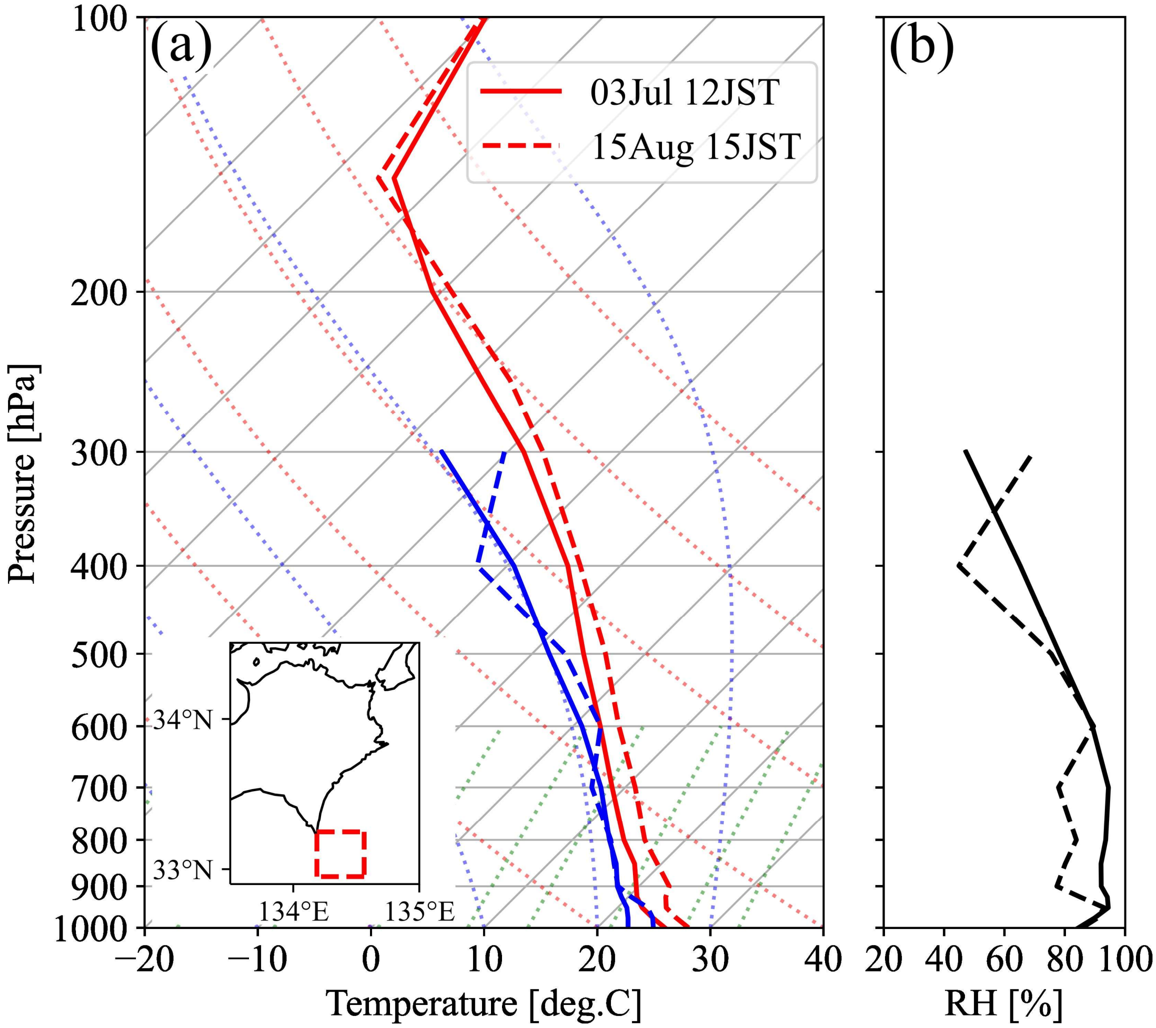

Fig. 6 (a) Skew-T log-p diagram collected from the initial value of JMA-MSM. Red and blue solid lines in (a) indicate vertical profiles of temperature [°C] and dew-point temperature [°C], respectively. Solid lines (dashed lines) represent the profile for 12 JST on July 3, 2018 (15 JST on August 15, 2018). Each value is a horizontal average within a red dashed rectangle (0.375°×0.3°) shown in the lower-left map. (b) Vertical profiles of relative humidity [%] obtained at the same time and location as (a). The solid and dashed lines have the same meanings as those in (a).

Fig. 7

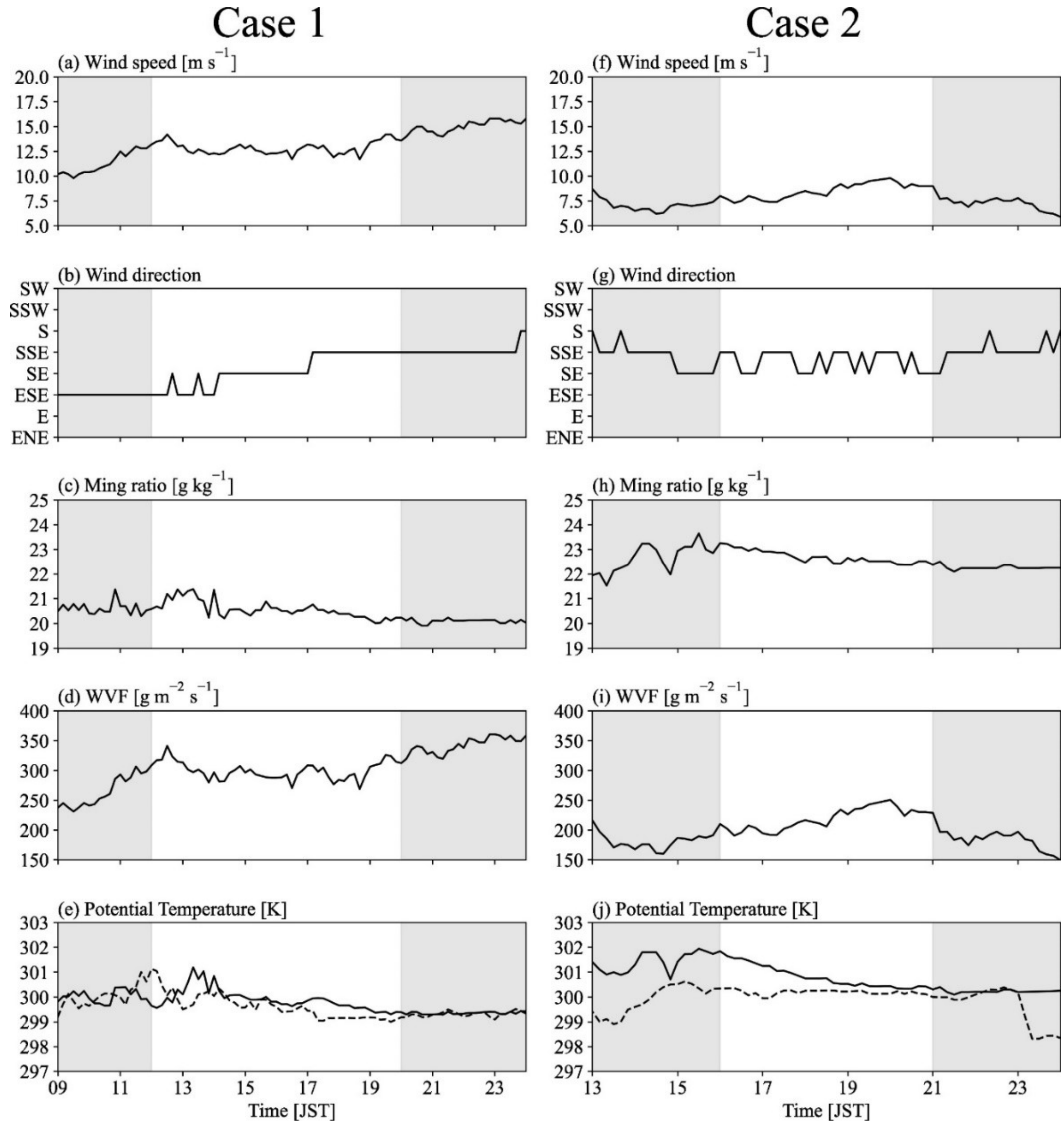

Fig. 7 Time series of (a) wind speed [m s^{-1}], (b) wind direction, (c) water vapor mixing ratio [g kg^{-1}], (d) water vapor flux (WVF) [g kg^{-1} s^{-1}], and (e) potential temperature [K] observed by JMA surface weather station at Murotomisaki (solid line) and Kaiyo (dashed line, only shown in potential temperature) from 09 to 24 JST on July 3, 2018. (f)–(j) Same as (a)–(e), but for from 13 to 24 JST on August 15, 2018. The gray-shaded periods represent times beyond the scope of this study. The locations of Murotomisaki and Kaiyo are shown in Fig. 1.

Fig. 8

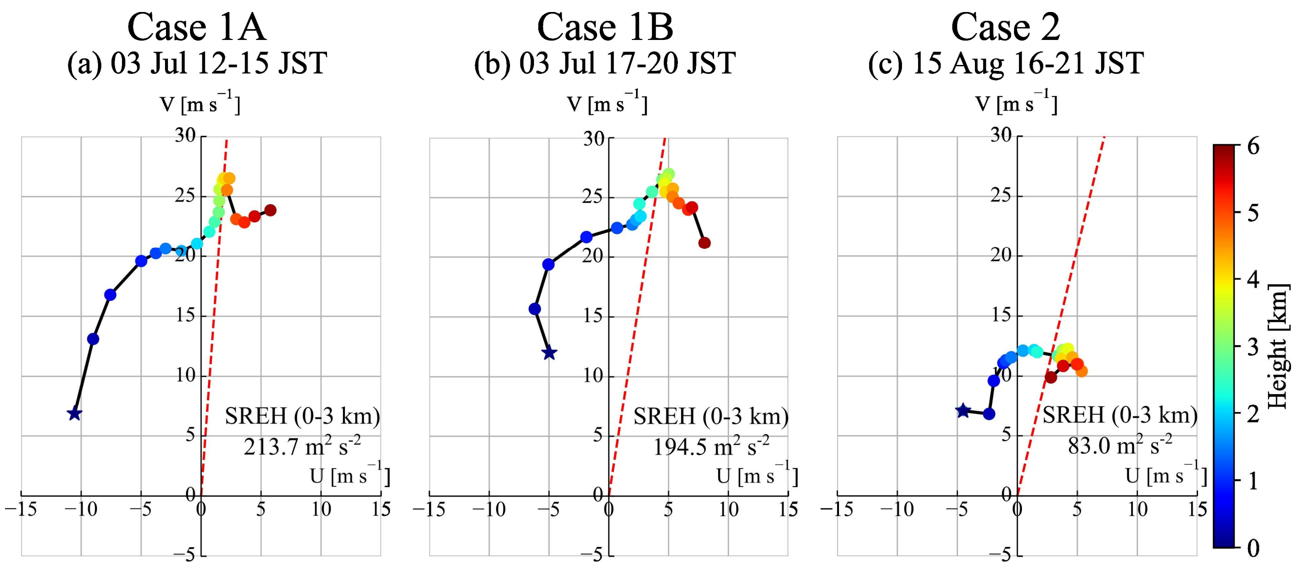

Fig. 8 Hodographs of horizontal wind [m s^{-1}] observed by JMA wind profiler radar at Kochi (circles) and JMA surface weather station at Murotomisaki (stars) averaged during (a) Case 1A (12 to 15 JST on July 3, 2018), (b) Case 1B (17 to 20 JST on July 3, 2018), and (c) Case 2 (16 to 21 JST on August 15, 2018). The colors of plots indicate the observation height (291 m intervals, except for the surface to the lowest wind profiler radar plot (109 m)). Red dashed lines indicate the orientation angles of the Muroto Lines obtained by averaging the orientations of hourly rainfall area 20 mm or grater during each period.

Fig. 9

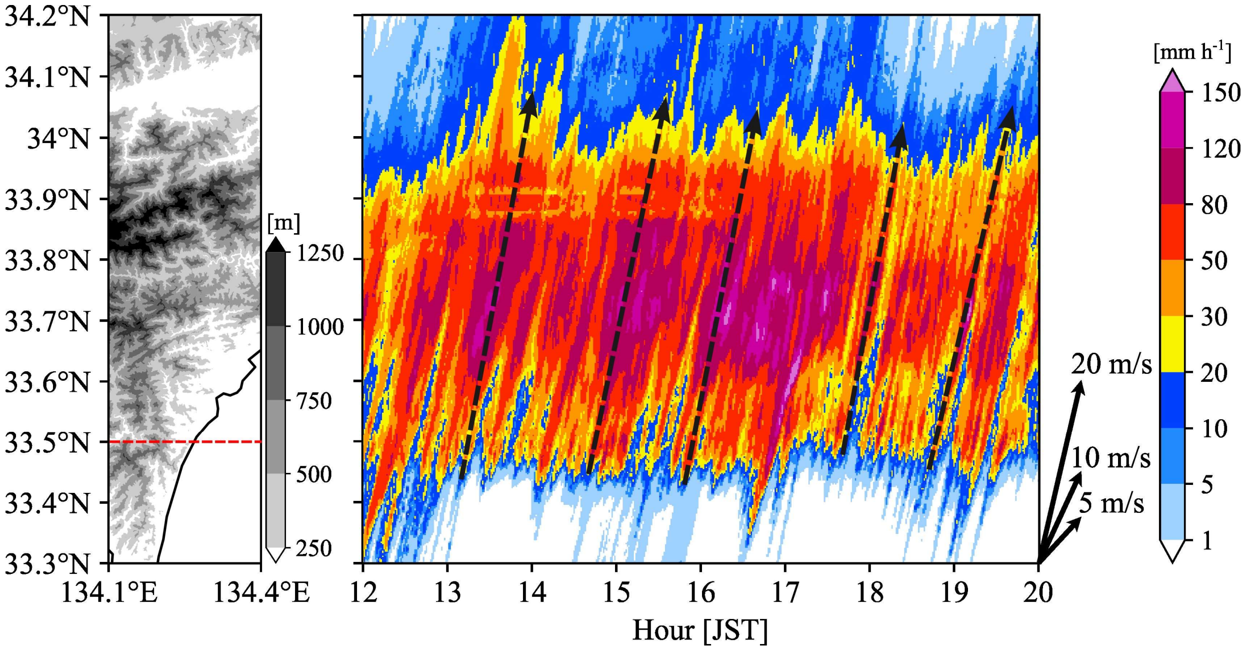

Fig. 9 Time-latitude section of maximum rainfall intensity [mm h^{-1}] between 134.1°E and 134.4°E obtained from XRAIN during Case 1 (from 12 JST to 20 JST on July 3, 2018). The orography in the analyzed area is shown on the left panel. The orientation of solid-arrows on the lower-right corner of figure indicates the representative meridional moving speed of convective cells. Dashed-arrows represent the meridional movement of several convective cells. A red-dashed line in the left panel indicates the latitude of a time-longitude cross section shown in Fig. 11a.

Fig. 10

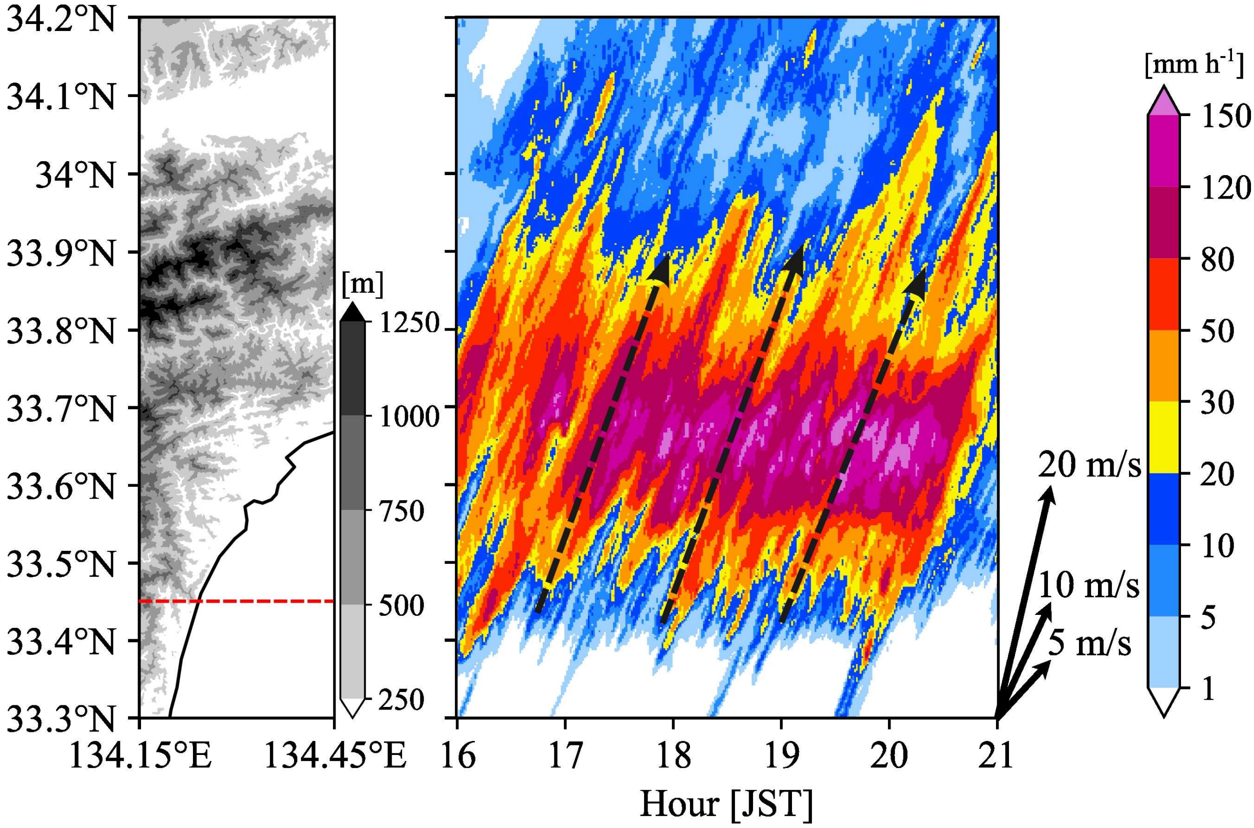

Fig. 10 Same as Fig. 9, but for maximum rainfall intensity [mm h^{-1}] between 134.15 °E and 134.45 °E during Case 2 (from 16 JST to 21 JST on August 15, 2018). A red-dashed line in the left panel indicates the latitude of a time-longitude cross section shown in Fig. 11a.

Fig. 11

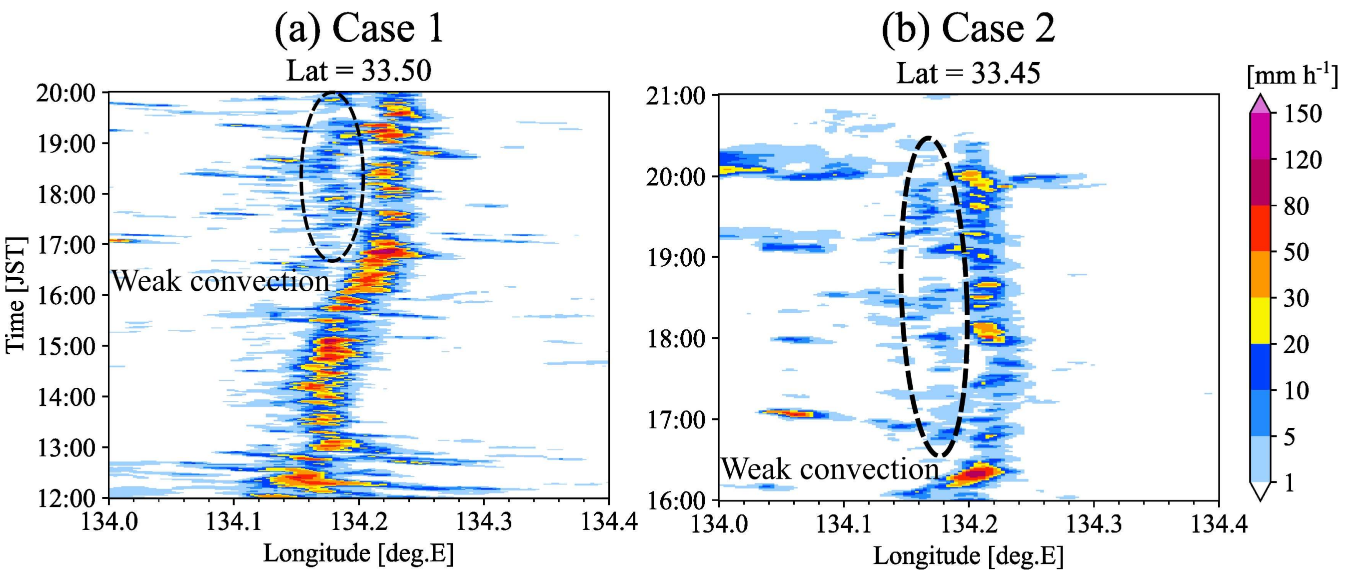

Fig. 11 Time-longitude cross section of XRAIN rainfall intensity [mm h^{-1}] (a) at 33.50°N during Case 1 (from 12 to 20 JST on July 3, 2018) and (b) at 33.45°N during Case 2 (from 16 to 21 JST on August 15, 2018). Black dashed circles indicate a weak convection formed west of the Muroto Line.

Fig. 12

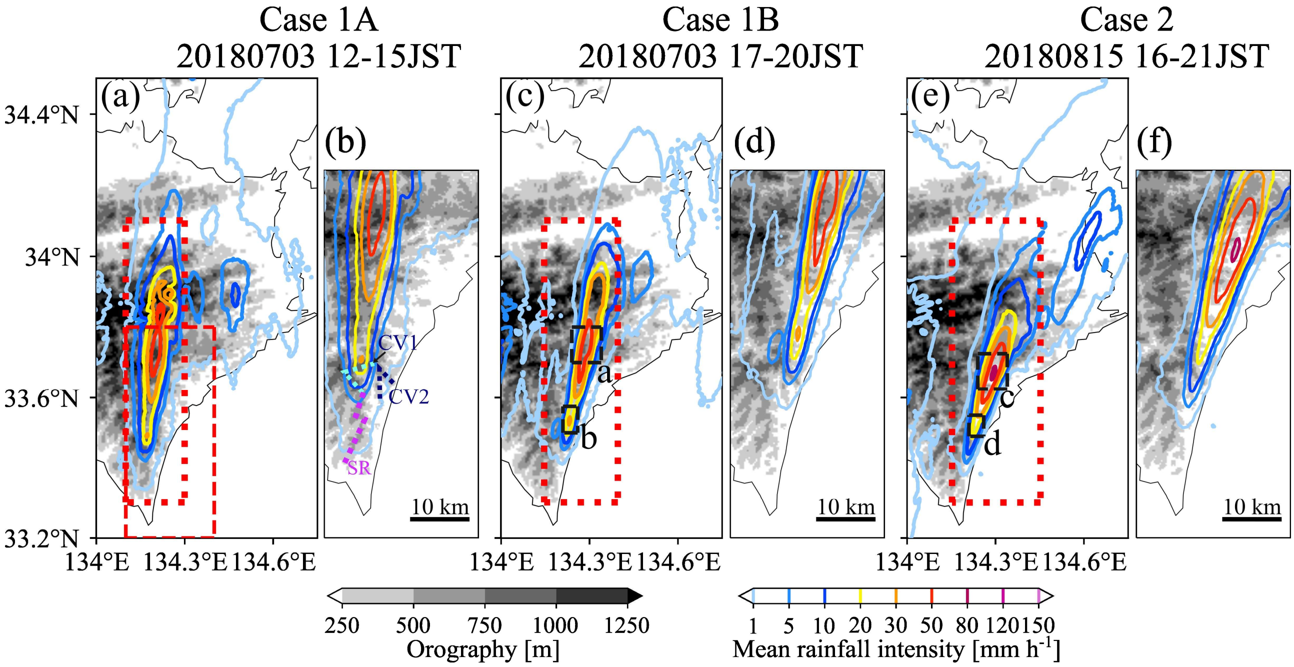

Fig. 12 Horizontal distribution of mean rainfall intensity [mm h^{-1}] (colored contour) derived from XRAIN and orography [m] (shaded) for (a) Case 1A (from 12 to 15 JST on July 3, 2018). A red-dashed rectangle indicates the displaying area of (b), (d), and (f). A red-dotted rectangle shows the analysis area of Fig. 13. (b) Enlarged display of (a) focusing on the southern part of the Muroto Line. Purple-dotted line displays the location of the SR small-scale ridge. Light- and dark-blue-dotted lines indicate locations of small-scale concave valleys named CV1 and CV2, respectively. (c) (d) Same as (a) and (b), respectively, but for Case 1B (from 17 to 20 JST on July 3, 2018). (e) (f) Same as (a) and (b), respectively, but for Case 2 (from 16 to 21 JST on August 15, 2018). Black-dashed rectangles and alphabets in (c) and (e) represent CFAD analyses areas and subcaptions in Fig. 14.

Fig. 13

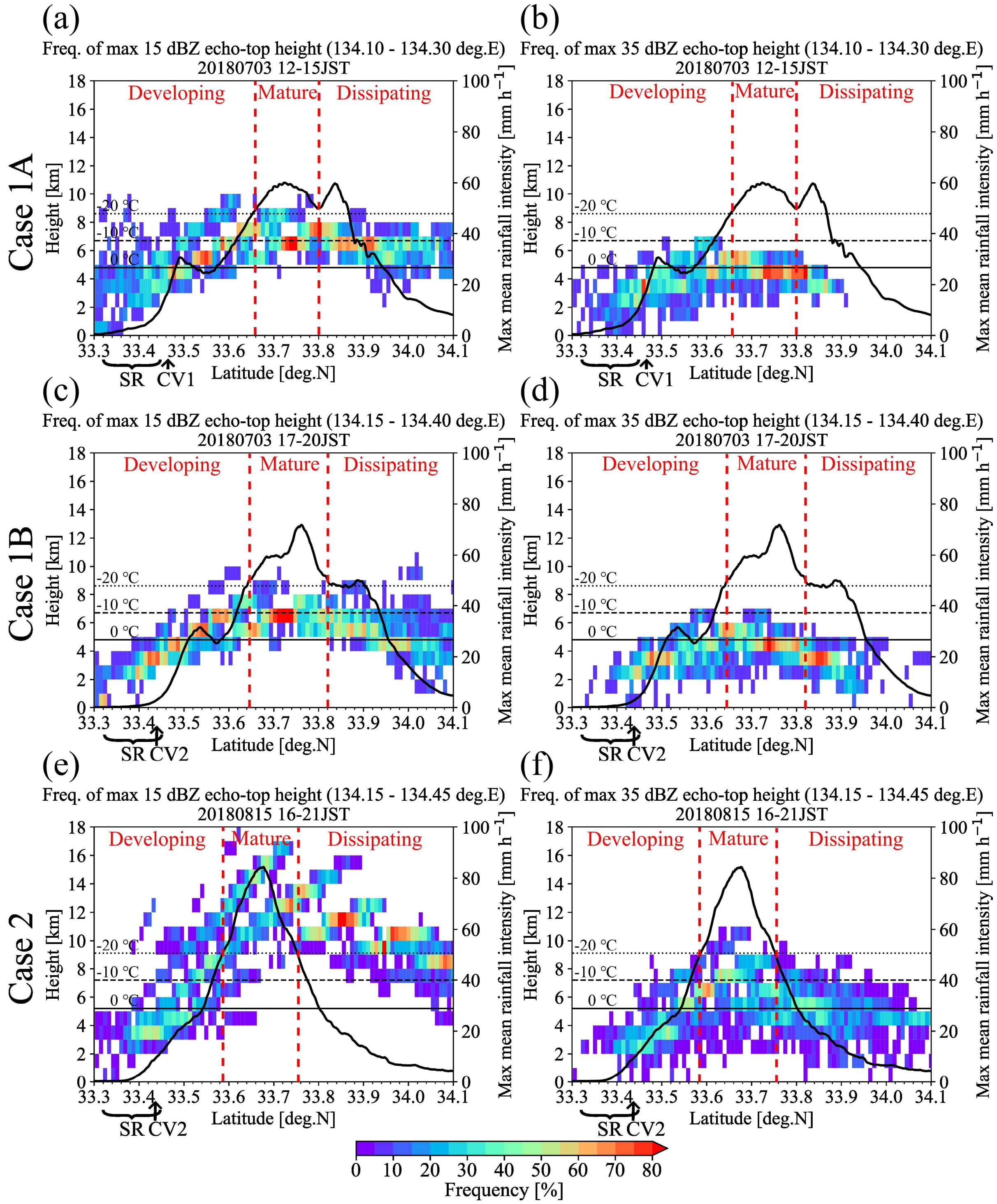

Fig. 13 Appearance frequency of the zonal maximum echo-top height obtained from JMA Murotomisaki CAPPI data [%] (shaded) and the zonal maximum value of mean XRAIN rainfall intensity [mm h^{-1}] (black solid curve lines). (a) (b) Maximum 15 dBZ and 35 dBZ

echo-top height between 134.10°E and 134.25°E during Case 1A (from 12 to 15 JST on July 3, 2018), respectively. Solid, dashed, and dotted horizontal lines show the 0°C, -10°C, and -20°C height derived from Fig. 6, respectively. Red-dashed lines indicate boundaries between the developmental stages of typical convective cells of the Muroto Lines. The locations of SR and concave valleys (CV1 or CV2) beneath the Muroto Lines are indicated by brackets and arrows, respectively. (c) (d) Same as (a) and (b), respectively, but for the maximum values between 134.15°E and 134.40°E during Case 1B (from 17 to 20 JST on July 3, 2018). (e) (f) Same as (a) and (b), respectively, but for the maximum values between 134.15°E and 134.45°E during Case 2 (from 16 to 21 JST on August 15, 2018).

Fig. 14

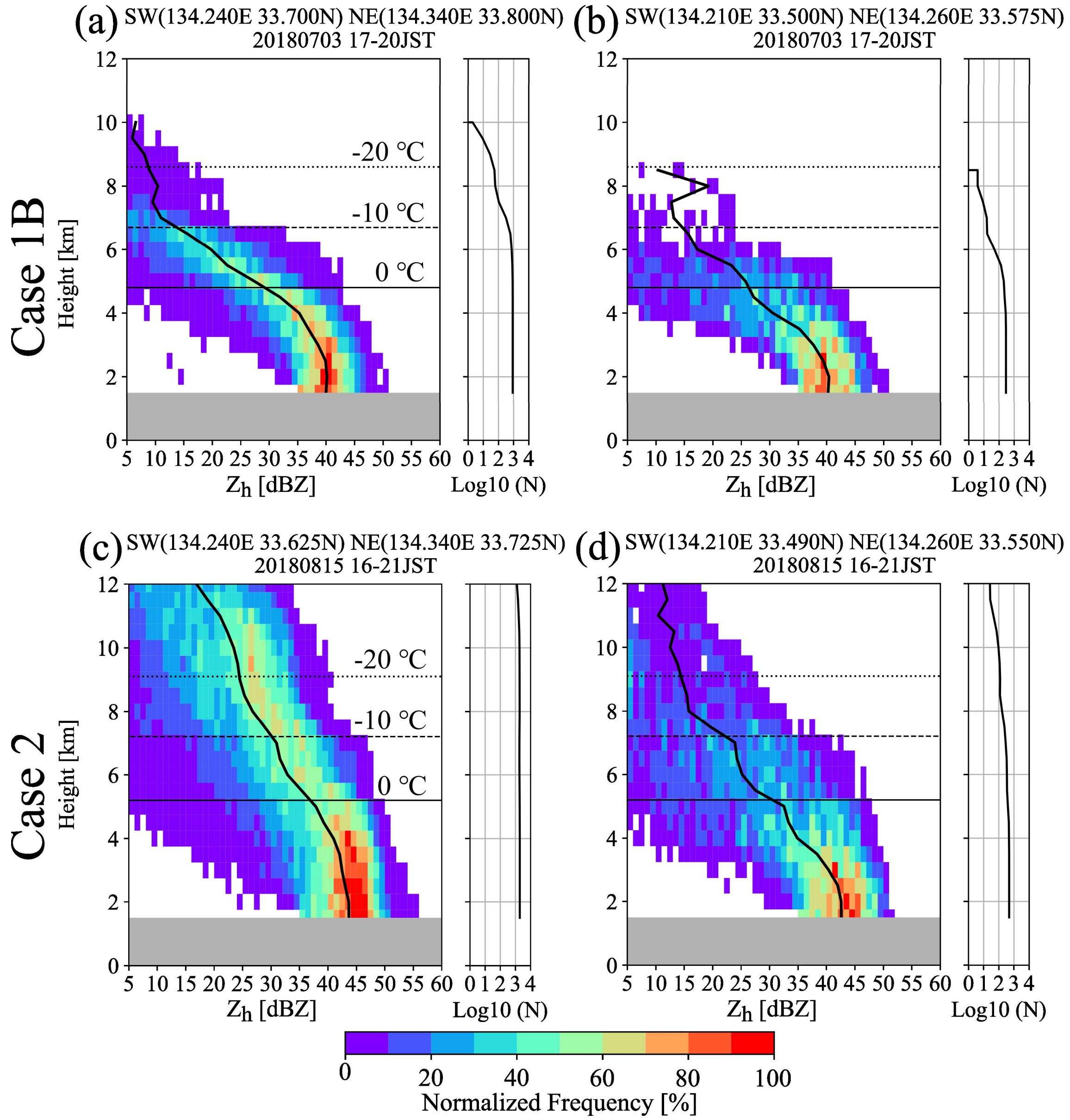

Fig. 14 Normalized Contoured Frequency by Altitude Diagrams (CFADs) of horizontal reflectivity (Z_h) obtained from JMA Murotomisaki CAPPI data [%] sampled at (a) the strongest rainfall area, (b) the southernmost part of the intense rainfall area during Case 1B (from 17 to 20 JST on July 3, 2018). The analysis areas of each figure are displayed in Fig. 12. Bold solid curve lines indicate the vertical profile of the median of Z_h. The thin solid, dashed, and dotted horizontal lines show the 0°C, -10°C, and -20°C levels derived

from Fig. 6, respectively. The data below 1.5 km in height is masked by gray shade due to the lack of observation. The right panel of each figure shows the logarithmic number of samples at each height. (c), (d) same as (a) and (b) respectively, but during Case 2 (from 16 to 21 JST on August 15, 2018).

Fig. 15

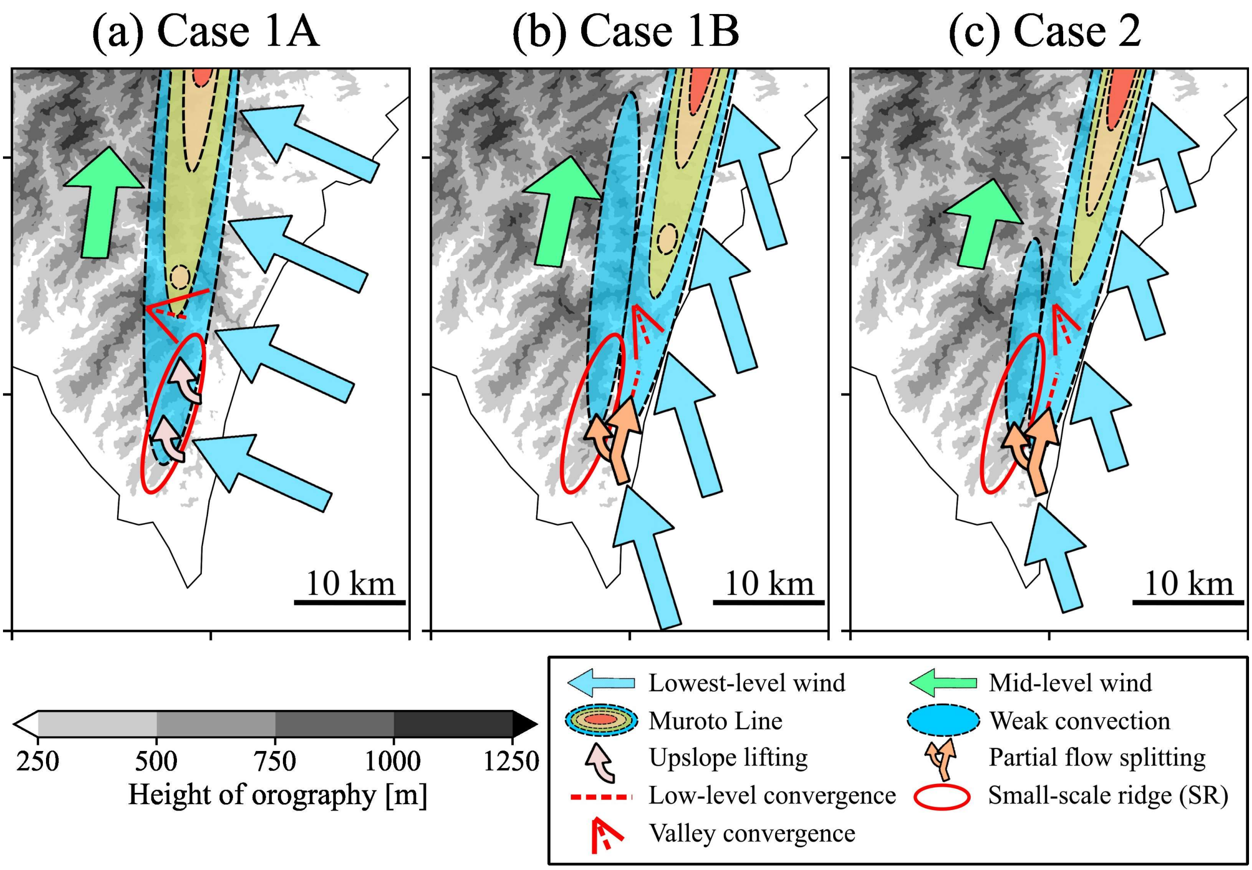

Fig. 15 Schematic diagrams of the airflow structures and orography that contribute to the maintenance and development of the Muroto Lines suggested in this study. (a) Case 1A. The background shade indicates height of orography. The meanings of arrows, ellipses, and lines are shown in the legend (see text for the details of each element). (b) Same as (a), but for Case 1B. (c) same as (b), but for Case 2.

Fig. A1

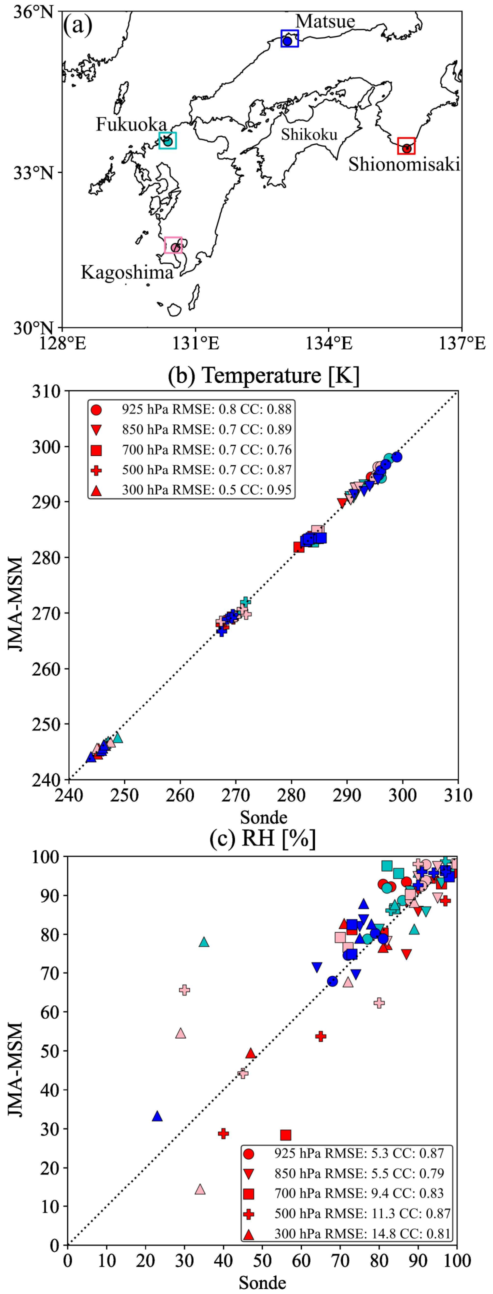

Fig. A1 (a) Locations of soundings stations used for the comparison with the JMA-MSM data. Circles and squares indicate the locations of sounding stations and averaging areas for the JMA-MSM (0.375°×0.3°), respectively. (b) Scatter plot comparing temperatures [K] from the soundings and the JMA-MSM data. The symbols represent data at different pressure levels: circle (925 hPa), inverted triangle (800 hPa), square (700 hPa), plus (500 hPa), and triangle (300 hPa). The colors correspond to the comparison locations: red (Shionomisaki), dark-blue (Matsue), light-blue (Fukuoka), and pink (Kagoshima). ‘RMSE’ and ‘CC’ in the legend denote root mean square error and correlation coefficient calculated for each level, respectively. (c) Same as (b), but for relative humidity [%].